



1 **Urban Area Observing System (UAOS) Simulation**
2 **Experiment Using DQ-1 Total Column Concentration**
3 **Observations**

4 Jinchun YI¹, Yiyang Huang¹, Zhipeng Pei², Ge Han^{1,*}

5 ¹Hubei Key Laboratory of Quantitative Remote Sensing of Land and Atmosphere, School of Remote
6 Sensing and Information Engineering, Wuhan University, Wuhan, China

7 ²State Key Laboratory of Information Engineering in Surveying, Mapping and Remote Sensing, Wuhan
8 University, Wuhan, China

9 *Correspondence to:* Ge Han (udhan@whu.edu.cn)

10 **Abstract.** Satellite observations of the total column dry-air CO₂ (XCO₂) have been proven to support
11 the monitoring and constraining of fossil fuel CO₂ (ffCO₂) emissions at the urban scale. We utilized the
12 XCO₂ retrieval data from China's first laser carbon satellite dedicated to comprehensive atmospheric
13 environmental monitoring, DQ-1, in conjunction with a high-resolution transport model and a Bayesian
14 inversion system, to establish a system for quantifying and detecting CO₂ emissions in urban areas.
15 Additionally, we quantified the impact of uncertainties from satellite measurements, transport models,
16 and biospheric fluxes on emission inversions. To address uncertainties from the transport model, we
17 introduced random wind direction and speed errors to the ffCO₂ plumes and conducted 10⁴ simulations
18 to obtain the error distribution. In our pseudo-data experiments, ODIAC overestimated fossil fuel
19 emissions for Beijing and Riyadh, while underestimating emissions for Cairo. Specifically, we simulated
20 Beijing and leveraged DQ-1's active remote sensing capabilities, utilizing its rapid day-night revisit
21 ability. We assessed the impact of daily biospheric fluxes on ffXCO₂ enhancements and further analyzed
22 the diurnal variations of biospheric flux impacts on local XCO₂ enhancements using three-hourly
23 average NEE data. The results indicate that a significant proportion of local XCO₂ enhancements are
24 notably influenced by biospheric CO₂ variations, potentially leading to substantial biases in ffCO₂
25 emission estimates. Moreover, considering biospheric flux variations separately under day and night
26 conditions can improve simulation accuracy by 20-70%. With appropriate representations of uncertainty
27 components and a sufficient number of satellite tracks, our constructed system can be used to quantify
28 and constrain urban ffCO₂ emissions effectively.

29 **1 Introduction**

30 More than 170 countries have signed the Paris Agreement, vowing to keep the global average temperature
31 increase within 2 degrees Celsius in this century. Accurate carbon accounting is the basis for any
32 mitigation measures. Over 70% of the anthropogenic CO₂ emissions are from urban areas (Biroi, 2010).

33 It is thus critical to develop effective means to estimate urban CO₂ emissions accurately. "bottom-up"
34 (inventory) approaches have shown good performances in developed countries such as U.S.A and E.U



35 (Crippa et al., 2018; Kevin R Gurney et al., 2009). However, huge uncertainties in estimation of
36 anthropogenic CO₂ emissions are inevitable in developing countries such as China and India because of
37 the booming economics and imperfect monitoring systems. For example, the discrepancy between
38 different estimations of CO₂ emissions of China exceeded 1,770 million tones (20%) in 2011(Shan et al.,
39 2016), which is approximately equal to the Russian Federation's total emissions in 2011(Shan et al.,
40 2018). Therefore, "top-down" (inverse) approaches could play a more significant role in those countries
41 to estimate and update carbon fluxes. In addition, carbon emission inventories with a spatial resolution
42 of 0.1° are available at the global scale (Janssens-Maenhout et al., 2017; Oda & Maksyutov, 2011),
43 however, Oda et al warned that available information is insufficient to fully evaluate the relationship
44 between CO₂ emission and the proxy data, such as population and nightlight(Oda & Maksyutov, 2011).
45 Consequently, associated errors would increase at finer resolutions. On the other hand, the anthropogenic
46 carbon emissions are assumed to be known quantities and are important as reference for analyzing a
47 budget of the three fluxes(Kevin Robert Gurney et al., 2005; K. R. Gurney et al., 2002). Therefore, there
48 is an urgent need to develop novel methods to acquire more robust and accurate surface CO₂ fluxes with
49 fine resolution in urban areas where the majority of anthropogenic CO₂ emissions locate.

50 The atmospheric inversion technique has been widely used to retrieve carbon fluxes at large geographic
51 scales (Bakwin et al., 2004; Ballantyne, Alden, Miller, Tans, & White, 2012; Bousquet, Ciais, Peylin,
52 Ramonet, & Monfray, 1999; Breon & Peylin, 2003; Gerbig et al., 2003; Myneni et al., 2001; Stephens et
53 al., 2007; Watson et al., 2009), by using measurements from the network of ground-based greenhouse
54 gas stations. Dense and accurate observations of CO₂ dry-air mixing ratios (x_{CO_2}) are needed to inverse
55 carbon fluxes at a finer geographic scale (Kaminski et al., 2017; Rayner & O'Brien, 2001), enabling
56 smaller-scale sources emitting CO₂ into the atmosphere to be better quantified (A. Eldering, C. W. O'Dell,
57 et al., 2017). Remote sensing from space is undoubtedly the most appropriate means to obtain dense CO₂
58 observations rapidly in large extents (Buchwitz et al., 2017; Ehret et al., 2008). GOSAT and OCO-2
59 provide us an opportunity to retrieve column-average x_{CO_2} (X_{CO_2}) globally except in Polar Regions.
60 Recent studies have demonstrated the promising potential of OCO-2 to help scientists identify localized
61 CO₂ sources (Schwandner et al., 2017) , estimate regional CO₂ fluxes (A. Eldering, P. O. Wennberg, et
62 al., 2017) and map the gross primary production (Kohler, Guanter, Kobayashi, Walther, & Yang, 2018;
63 Li, Xiao, & He, 2018; Sun et al., 2018). It is still a challenging mission to obtain accurate estimates of



64 CO₂ fluxes using X_{CO₂} products, especially in urban areas, because the signals received by OCO-
65 2/GOSAT need to be attributed unambiguously to variations in atmospheric CO₂ concentration, as
66 opposed to variations caused by environmental factors such as aerosols and clouds (J. B. Miller, P. P.
67 Tans, & M. Gloor, 2014). Along with the success of passive remote sensing of CO₂, U.S.A and China are
68 ambitious to send their LIDAR sensors into the orbit to realize monitoring CO₂ in all latitudes and in
69 nights (Abshire et al., 2017; Han et al., 2017a). Effect of aerosols and thin clouds on retrievals of X_{CO₂}
70 can be eliminate through a differential process of signals from two very close wavelengths (Amediek,
71 Fix, Wirth, & Ehret, 2008; Han, Gong, Lin, Ma, & Xiang, 2015; Mao et al., 2018). Therefore, a smaller
72 bias of retrievals of CO₂-IPDA LIDAR is expected comparing with the passive remote sensing, which is
73 beneficial for inversion of CO₂ fluxes. Previous studies had focused on performance evaluation of CO₂-
74 IPDA LIDARs in terms of systematic errors, random errors as well as the coverage (Ehret et al., 2008;
75 Han et al., 2017a; Kawa et al., 2010). There are evident differences between X_{CO₂} products of OCO-2
76 and those of the forthcoming CO₂-IPDA LIDAR in terms of coverage patterns (Kawa et al., 2010; C.
77 Kiemle, Kawa, Quatrevalet, & Browell, 2014; C. Kiemle et al., 2011). Unlike the passive remote sensing
78 of CO₂ that can scan perpendicular to the direction of the satellite orbit, IPDA LIDAR in practice has
79 sensors that only operate in point mode due to the unaffordable power consumption and cost of
80 implementing a scan mode. Such a difference can be ignored when one tries to estimate large scale CO₂
81 fluxes by using satellite-derived XCO₂ products with a resolution of 1° (or coarser). However, specific
82 inversion methods, which take the characteristics of LIDAR products into considerations, are urgently
83 needed for inversion of fine scale CO₂ fluxes (Christoph Kiemle et al., 2017). Our previous work has
84 already confirmed that it is feasible to retrieve X_{CO₂} in urban areas using the CO₂-IPDA LIDAR (ACDL)
85 which will be onboard on the Atmospheric Environment Monitoring Satellite (AEMS) DQ-1 of China
86 (Han et al., 2018). In this work, an inversion framework is used to inverse fine scale (~1 km/0.01°) CO₂
87 fluxes of urban areas using pseudo XCO₂ observations from ACDL. Our main objective is to figure out
88 the ability and potential of ACDL to help us estimate anthropogenic carbon emission in urban areas. In
89 turn, results of the performance evaluation will be the justification for improve the configuration of the
90 ongoing ACDL and its successor which would be sent to the orbit in just 2-3 years after AEMS.
91 Though positive relationship between satellite-derived XCO₂ anomalies/enhancements and CO₂
92 emissions has been witnessed (Hakkarainen, Ialongo, & Tamminen, 2016), it is by no means a forgone



93 conclusion that CO₂ sources and sinks can now be measured from space at high resolution (J. B. Miller
94 et al., 2014). Atmospheric transport models are indispensable to build a bridge between CO₂
95 sources/sinks and measured concentrations (Rayner & O'Brien, 2001). Stochastic Time-Inverted
96 Lagrangian Transport (STILT) was invented in 2003 (J. C. Lin et al., 2003) and soon was utilized to
97 inverse fluxes of trace gases (Gerbig et al., 2003; J. C. Lin et al., 2004). In 2010, Weather Research and
98 Forecasting (WRF) model was coupled with STILT (WRF-STILT), offering an attractive tool for inverse
99 flux estimates (Nehrkorn et al., 2010). Since then, several scientists utilized this effect tool to model CO₂
100 distribution and inverse CO₂ fluxes using in-situ measurements (Kort, Angevine, Duren, & Miller, 2013;
101 Nehrkorn et al., 2013; Pillai et al., 2012; Vogel et al., 2013) as well as satellite observations (Reuter et
102 al., 2014; Turner et al., 2018; J. S. Wang et al., 2014). Recently, STILT was further updated to facilitate
103 modeling of trace gases with a fine scale (Fasoli, Lin, Bowling, Mitchell, & Mendoza, 2018). The key
104 product provided by WRF-STILT is the “footprint” which describes the sensitivity of measurements
105 (receptors) to surface fluxes in upwind regions. Then, the Bayesian inversion method can be used along
106 with the footprint and a-priori surface fluxes to estimate a-posterior surface fluxes.

107 In this study, we propose a framework based on DQ-1 XCO₂ data to periodically assess urban-scale fossil
108 fuel CO₂ emissions. We employ Observing System Simulation Experiments (OSSEs) to investigate the
109 performance of DQ-1's ACDL XCO₂ products in improving CO₂ flux estimation at an enhanced spatial
110 resolution of $0.01^\circ \times 0.01^\circ$ over urban areas. The OSSE consists of a forward simulation module and an
111 inversion framework. The forward module utilizes WRF modeling for high-resolution simulations,
112 allowing us to capture fine-scale gas particle transport characteristics and variations. We simulate pseudo-
113 measurements and corresponding errors based on hardware configurations, environmental parameters,
114 and physical process simulations within this module. The inversion framework relies on footprints
115 provided by WRF-STILT to estimate urban-scale emission scaling factors using Bayesian inversion
116 methods. The study also accounts for the impacts of measurement errors, transport model uncertainties,
117 and biosphere flux uncertainties on emission estimation uncertainty throughout the OSSE. Initially, we
118 evaluate emission estimation uncertainty related to transport model and measurement errors, focusing on
119 three cities: Beijing, Riyadh, and Cairo, each with distinct topographical influences. Riyadh and Cairo
120 exhibit negligible local biosphere flux impacts on emission estimates due to relatively flat terrain and
121 stable wind fields, categorizing them as "plume cities" where CO₂ emissions are typically captured in



122 plume forms due to these conditions (Ye et al., 2020). Building on these simulations, we conduct OSSEs
123 to assess the potential of using XCO₂ data from multiple DQ-1 orbits to track urban emissions regularly.
124 Leveraging DQ-1's unique day-night revisit capability, we also evaluate uncertainties arising from local
125 biosphere flux variations in Beijing. Unlike previous inversion studies using OCO-2/3, which primarily
126 sample during daytime, DQ-1's day-night orbit allows for more evenly distributed temporal sampling.
127 Furthermore, combining DQ-1's day-night revisit capability, we introduce for the first time an analysis
128 of how biosphere flux variations between day and night affect emission estimates using forward
129 simulations and Bayesian inversion. Lastly, we summarize the significance of future satellite
130 observations in monitoring urban emissions.

131 **2 Data and method**

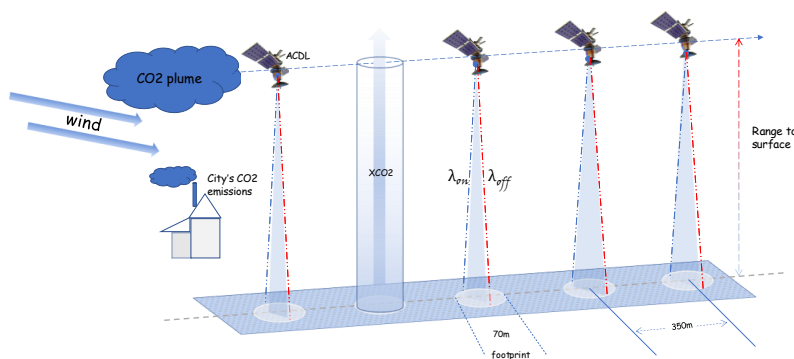
132 **2.1 ACDL XCO₂ products**

133 In order to design a device similar to the Cloud-Aerosol Lidar with Orthogonal Polarization (CALIOP)
134 onboard the CALIPSO satellite, the design of DQ-1 was initially proposed in 2012. It was officially
135 approved in 2017. Distinct from other environmental monitoring satellites, a notable and innovative
136 highlight of DQ-1 is the integration of a lidar payload for space-based top-down CO₂ detection, known
137 as ACDL. In subsequent developments, ACDL underwent a series of laboratory prototype developments
138 (Zhu et al., 2019) and airborne prototype testing missions (Q. Wang et al., 2021; Xiang et al., 2021; Zhu
139 et al., 2020). Finally, ACDL was launched into a near-Earth sun-synchronous orbit at an altitude of
140 approximately 705 kilometers on April 18, 2022. ACDL began data collection in late May 2022 and
141 officially commenced operations. This study primarily utilizes data from June 2022 to April 2023 for
142 further research.

143 ACDL employs standard IPDA lidar technology, using differential absorption methods to acquire column
144 concentrations of atmospheric carbon dioxide (CO₂). A detailed description of the XCO₂ detection
145 algorithms and products is in preparation. In this paper, we briefly introduce its detection principles.
146 ACDL emits a pair of nearly simultaneous observation signals, one with a wavelength located at the
147 strong absorption position of the R16 line in the CO₂ spectrum (on-line wavelength) and the other at a
148 weak absorption position of the same line (off-line wavelength). The on-line and off-line wavelengths



149 are stabilized at 6361.225 cm⁻¹ and 6360.981 cm⁻¹, corresponding to 1572.024 nm and 1572.085 nm,
150 respectively. This slight wavelength difference enables ACDL to counteract interference from aerosols
151 and other molecules, excluding water vapor, through the differential process of the reflected signals. The
152 detection of XCO₂ by ACDL is calculated based on specific algorithms (see Section 2.4.1).



153

154 **Figure 1: the schematic diagram for DQ-1's detection principle**

155 Figure 1 illustrates the detection principle of DQ-1. The XCO₂ products generated by ACDL are similar
156 to those of GOSAT, adopting a point sampling mode. The lidar operates in nadir observation mode, with
157 approximately one 70-meter footprint observed every 350 meters along the track.

158 According to Equation 1, we calculate XCO₂ by directly using the normalized weighting function (IWF).
159 Significant differences in XCO₂ measurements can be observed between ACDL and OCO-2/3. Currently,
160 passive remote sensing satellites like OCO-2/3 and GOSAT estimate XCO₂ by measuring the solar
161 spectrum and using a priori information guided by optimal estimation theory to derive xco2(p), ultimately
162 obtaining XCO₂ (J. B. Miller, P. P. Tans, & M. J. N. G. Gloor, 2014). In contrast to these traditional
163 passive optical remote sensing satellites, ACDL does not 'estimate' xco2(p) but directly 'calculates' the
164 weighted average column concentration (Zhang et al., 2024). During the integration phase of ACDL's
165 development, we evaluated the WF shapes of various on-line wavelengths and selected one that responds
166 strongly near the surface and weakly at higher altitudes (Han et al., 2017b). This design allows changes
167 in surface CO₂ concentration, driven by surface CO₂ fluxes, to be more prominently reflected in the



168 column concentration. Therefore, this WF enhances the ability to identify surface CO₂ variations and
169 provides more information for subsequent CO₂ flux inversion.

170 **2.2 Study Area**

171 Considering the available orbital tracks for DQ-1 inversion, vegetation coverage, and the complexity of
172 meteorological conditions, this paper selects three cities and regions to highlight the different sources of
173 uncertainty in emission inversion and the inversion capability of DQ-1. The selected cities share the
174 following characteristics: 1) high fossil fuel emissions; 2) typical "plume cities," characterized by
175 ffXCO₂ enhancements distributed in plume forms (Deng et al., 2017). Riyadh, with a population of 8
176 million, and Cairo, with a population of 20 million, have significantly weaker biosphere contributions
177 compared to Beijing. In subsequent research, it is considered that the spatial gradient of biosphere CO₂
178 flux can be ignored compared to local fossil fuel emissions.

179 To assess the impact of biosphere flux uncertainty on the inversion process and separately evaluate the
180 impact of daytime and nighttime biosphere flux on the simulated local XCO₂ enhancement, we selected
181 Beijing, the capital city of China, with a population of approximately 21.5 million. Beijing is not only
182 the political center of China but also one of the most populous cities. Compared to its surrounding areas,
183 Beijing has relatively less vegetation. Surrounding cities might have better-preserved natural ecological
184 environments and more abundant vegetation cover due to less industrialization and urbanization. For
185 instance, the mountainous and suburban areas around Beijing may have more forests, grasslands, and
186 farmlands, whereas green spaces within Beijing are often limited to parks, green belts, and a few nature
187 reserves. As a city with high fossil fuel emissions and active biosphere exchange, Beijing is well-suited
188 for studying the impact of biosphere flux uncertainty on emission estimates.

189 **2.3 Atmosphere Mode Setting**

190 **2.3.1 WRF-STILT**

191 The spatial heterogeneity of emissions and dense point sources (such as power plants) lead to a complex
192 spatial structure of urban emissions, resulting in intricate ffCO₂ plumes combined with local atmospheric
193 dynamics. To explore fine-scale urban emission patterns, this study employs the WRF-STILT model
194 (WRF: Weather Research and Forecasting, STILT: Stochastic Time-Inverted Lagrangian Transport). The



195 STILT Lagrangian model driven by WRF meteorological fields is characterized by a realistic treatment
196 of convective fluxes and mass conservation properties, which are crucial for accurate top-down estimates
197 of CO₂ emissions.

198 In this study's application of STILT, hourly outputs from version 4.0 of WRF are used to provide high-
199 resolution meteorological fields, with the model grid configured to 51 vertical (eta) layers. The 6-hourly
200 NCEP FNL (Final) global operational analysis data with a resolution of 1° are used as initial and boundary
201 conditions for meteorological and land surface fields to provide the initial and boundary conditions for
202 WRF runs. The simulations run for 30 hours, but only the 7th to 30th hours of each simulation are used
203 to avoid spin-up effects in the first 6 hours.

204 Each city uses the same one-way WRF nesting at 27 km, 9 km, and 3 km resolutions, with Riyadh
205 (23.7625° N, 45.7625° E - 25.4375° N, 27.4375° E), Cairo (29.1625° N, 30.4125° E - 30.8375° N, 32.0875° E), and Beijing
206 (39.4° N, 115.5° E - 41.075° N, 117.175° E) having their innermost regions used to filter DQ-1's orbital data. The
207 study area for STILT is set to be smaller than the innermost WRF region to eliminate the marginal effects
208 of WRF. Footprints quantitatively describe the contribution of surface fluxes from upwind areas to the
209 total mixing ratio at specific measurement locations, with units of mixing ratio per unit flux. The footprint
210 used in lidar satellite inversions is different from that used in general optical satellites, as detailed in
211 Section 2.4.1. STILT is configured to release 500 particles per receptor each time, with forward
212 dispersion over 24 hours. The particle release heights for STILT are set within the range of 50-1000 m,
213 with releases every 50 m, and 1000-2000 m, with releases every 100 m. Generally, as MAXAGL
214 increases from 1 km to 2 km, the urban enhancement increases and then stabilizes (Wu et al., 2021).

215

216 2.3.2 Inventory of Fossil Fuel Emissions

217 This article uses The Open-source Data Inventory for Anthropogenic CO₂ (ODIAC) which is a
218 global high-resolution fossil fuel carbon dioxide emissions (ffco₂) data product (Tomohiro Oda, 2015).
219 The 2023 version of ODIAC (ODIAC2023, 2000-2022) is based on the Appalachian State University's
220 Carbon Dioxide Information Analysis Center (CDIAC) team's (Gilfillan & Marland, 2021; Hefner,
221 Marland, Oda, & Change, 2024) most recent national ffco₂ estimates (2000-2020). The ODIAC
222 emissions inventory provides 1km × 1km global monthly average ffCO₂. The spatial decomposition of



223 emissions is accomplished using a variety of spatial proxy data, such as the geographic location of point
224 sources, satellite observations of night lights, and airplane and ship tracks. Seasonality of emissions was
225 obtained from the CDIAC monthly gridded data product (Andres et al., 2011) and supplemented using
226 the Carbon Monitor product (2020-2022, <https://carbonmonitor.org/>). In this paper, monthly data from
227 ODIAC are time-allocated, and neither the subsequent modeling nor the pseudo-data take into account
228 the daily and weekly time-variation of the ODIAC product.

229 2.3.3 Background XCO₂

230 To extract the XCO₂ enhancement for DQ-1 inversion, we define XCO₂ enhancement as entirely driven
231 by fossil fuel emissions. A classic method for extracting orbital background concentrations involves
232 selecting another "clean" orbit (minimally influenced by fossil fuel emissions) that is spatially and
233 temporally close, and using averaging or linear regression to approximate a background concentration
234 for the orbit under study. In this study, due to the fine-scale urban area emissions inversion, the study
235 area is small, making it challenging to find another clean orbit for calculating the background
236 concentration.

237 Previous studies have used inversion methods to derive background concentrations for orbits (Pei et al.,
238 2022), but these typically yield a background concentration for a region. These methods usually produce
239 a value unaffected by geographic location within a small area. However, for each orbit we study, a single,
240 constant background concentration is clearly unreasonable. Therefore, based on previous research, we
241 designed a simple and quick method to extract background concentrations, generating a background line
242 for each orbit of interest.

243 First, we perform a wavelet transform on DQ-1's XCO₂ data: $XCO_{DWT}^{Lidar} = DWT(XCO^{Lidar})$. Here, DWT
244 represents the discrete wavelet transform. The discrete wavelet transform can compress the DQ-1 data,
245 retaining the larger XCO₂ enhancements caused by fossil fuel emissions while attenuating enhancements
246 due to other factors. After the discrete wavelet transform, we assume that data exceeding a certain
247 threshold $mean(XCO_{DWT}^{Lidar}) + 0.5\sigma(XCO_{DWT}^{Lidar})$ is due to fossil fuel emissions and do not include these in the
248 background line calculation. We then perform a linear regression on the remaining data to extract the
249 background line.



250 **2.3.4 Biological Flux**

251 We specifically considered the influence of biogenic flux on the emission constraints in urban areas for
252 DQ-1. Two open-source NEE datasets were utilized in our study. The first dataset is derived from the
253 Carnegie-Ames-Stanford Approach-Global Fire Emissions Database Version 3 (CASA-GFED3) model
254 (Van der Werf et al., 2010), which provides 3-hourly average net ecosystem exchange (NEE) of carbon.
255 This dataset incorporates biogenic fluxes as well as fluxes associated with biomass burning emissions,
256 offering a global coverage of 3-hourly average NEE.

257 Additionally, we considered the ODIAC dataset, which provides advanced data-driven products on
258 global primary production, net ecosystem exchange, and ecosystem respiration (Jiye, 2020). The ODIAC
259 dataset offers 10-day average global NEE data and utilizes extensive ecosystem indices from MODIS
260 and ERA5 to deliver more precise data.

261 According to the study by (Ye et al., 2020), to better describe the diurnal variations and spatial distribution
262 of biogenic fluxes, the MODIS green vegetation fraction (GVF) was used to downscale the 3-hourly NEE
263 from the original grid resolutions ($0.5^\circ \times 0.625^\circ$ and $0.1^\circ \times 0.1^\circ$) to the WRF domain resolutions (27, 9,
264 and 3 km). This method assumes a linear relationship between carbon uptake and release and the
265 vegetation canopy coverage.

266 Our application of these datasets and downscaling methods enables a more accurate representation of
267 biogenic flux contributions to urban carbon emissions. By integrating high-resolution biogenic flux data,
268 we can improve the precision of emission inventories and enhance our understanding of urban carbon
269 dynamics. This approach allows us to better inform urban planning and policy-making aimed at reducing
270 carbon footprints and mitigating climate change impacts.

271 **2.4 Emission Optimization Method**

272 **2.4.1 Lidar Measurements as a Function of Flux: XSTILT-Lidar**

273 Unlike the XCO₂ products from passive satellites such as OCO-2/3, the XCO₂ product from DQ-1
274 (hereafter referred to as XCO₂^{Lidar} to distinguish it from passive satellite XCO₂ products) is derived using
275 the differential between on-wavelength (strong CO₂ absorption) and off-wavelength (weak CO₂
276 absorption) measurements. In this context, XCO₂^{Lidar} is obtained through the differential of the lidar



277 signals and integration weighting functions described in Section 2.1. Here, $WF(p)$ represents the lidar
 278 signal and p represents the pressure:

$$279 \quad XCO_2^{Lidar} = \frac{2 \cdot \ln\left(\frac{V_{off} \cdot V_{on-0}}{V_{on} \cdot V_{off-0}}\right)}{\int_{p_{surface}}^{p_{toa}} WF(p) dp} \quad 1$$

280 Here, V_{on} and V_{off} represent the reflected signal energies at the on-wavelength and off-wavelength,
 281 respectively, while V_{on-0} and V_{off-0} denote the transmitted signal energies. $p_{surface}$ indicates the
 282 atmospheric pressure at the laser ground point, and p_{top} represents the pressure at the top of the
 283 atmosphere. The denominator of Equation 1 represents the integration weighting function, as detailed in
 284 the study by (Refaat et al., 2016):

$$285 \quad WF(p) = \Delta\sigma_{wf}(\lambda_{on}, \lambda_{off}, p) \cdot N_{dry}(p) \quad 2$$

286 Here, $\Delta\sigma_{wf}(\lambda_{on}, \lambda_{off}, p)$ denote the CO₂ differential absorption cross-sections at the on-wavelength and
 287 off-wavelength, respectively. N_{dry} represents the number of dry air molecules per unit area in the pressure
 288 layer. This formula allows for the construction of the relationship between XCO_2^{Lidar} and the CO₂ profile
 289 $CO_2(p)$:

$$290 \quad XCO_2^{Lidar} = \frac{\int_{p_{surface}}^{p_{toa}} XCO_2(p) WF(p) dp}{\int_{p_{surface}}^{p_{toa}} WF(p) dp} = \frac{WF(p_1)}{IWF} \cdot CO_2(p_1) + \frac{WF(p_2)}{IWF} \cdot CO_2(p_2) + \dots \quad 3$$

291 Thus, the simulated enhancement in CO₂ emissions due to fossil fuels,
 292 $\Delta CO_{2,ffCO_2}(p) = \langle ffCO_2, foot(h) \rangle$, can be interpolated from the modeling results of CO₂ fluxes and
 293 tracer-tagged footprints. Therefore, a relationship between CO₂ fluxes and XCO_2^{Lidar} is established:

$$294 \quad XCO_2^{Lidar} - XCO_{2,background}^{Lidar} = \frac{WF(p_1)}{IWF} \cdot \langle ffCO_2, foot(h_1) \rangle + \frac{WF(p_2)}{IWF} \cdot \langle ffCO_2, foot(h_2) \rangle + \dots \quad 4$$

295 Here, $XCO_{2,ffCO_2,p}^{Lidar} = XCO_2^{Lidar} - XCO_{2,background}^{Lidar}$ represents the XCO₂ enhancement extracted from DQ-1
 296 observational data, and $XCO_{2,background}^{Lidar}$ represents the background concentration selected from the DQ-1
 297 orbit (detailed in Section 2.3.3). The symbol \langle, \rangle denotes the inner product operator, $ffCO_2$ is the prior
 298 emission flux, and $foot(h_n)$ represents the simulated footprints at different altitude layers. This formula
 299 establishes the mathematical foundation for inversion.

300 By integrating footprints from different release heights (Section 2.3.1 explains the selection of STILT

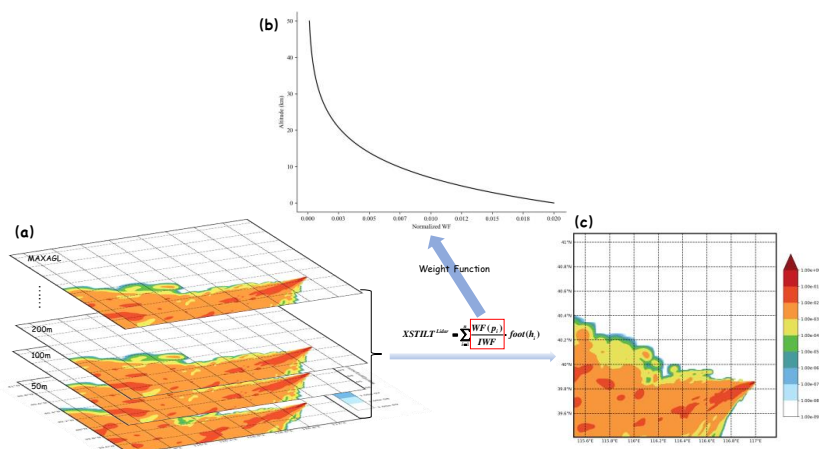


301 release heights), we further simplify the above equation. Here, we define $XCO2_{ffCO2,a}^{Lidar}$ as the XCO2
 302 enhancement simulated by the atmospheric transport model.

$$303 \quad XCO2_{ffCO2,a}^{Lidar} = \langle XSTILT^{Lidar}, ffCO2 \rangle \quad 5$$

$$304 \quad XSTILT^{Lidar} = \sum_{i=1}^n \frac{WF(p_i)}{IWF} \cdot foot(h_i) \quad 6$$

305 Here, we define $XSTILT^{Lidar}$ as the column-averaged footprint, corresponding to the column-averaged
 306 CO2 concentration. The inner product of the column-averaged footprint and the prior emission flux yields
 307 the simulated XCO2 enhancement. Thus, we can optimize the fossil fuel CO2 (ffCO2) emission
 308 parameters using the simulated and observed XCO2 enhancements to achieve the best consistency
 309 between the model and observed increments. By achieving this optimization, we ensure that the model
 310 accurately reflects the observed data, providing a reliable basis for further studies and policy-making.



311
 312 **Figure 2: Schematic diagram of XSTILT, Fig. (a) represents the simulated footprints at each horizontal**
 313 **altitude level we set (one footprint per 50m below 1000m, one footprint per 100m from 1000m-2000m, where**
 314 **MAXAGL represents the highest atmospheric altitude we simulate, which is 2000m) and the column average**
 315 **footprints obtained by integrating using the normalized integration function in Fig. (b). Figure (c).**

316 2.4.2 Optimization of Emission Constraint Factors

317 We adopted a Bayesian inversion method similar to that used by (Ye et al., 2020), which utilizes OCO-2
 318 observational data to constrain ffXCO2, aiming to achieve correlation between the model and observed
 319 ffXCO2 increments. Unlike the inversion of individual emission grids, we optimize emissions by



320 adjusting a scaling factor (λ) for the entire city's prior emissions without modifying each grid's flux
321 individually. The observational data along the DQ-1 orbit across all regions of interest serve as constraints
322 for the inversion, which can be expressed as:

$$323 \quad y_p = y_a \cdot \lambda + \varepsilon_p \quad 7$$

324 Here, y_p and y_a represent the observed and simulated ffXCO₂ enhancements, respectively. The term ε_p
325 denotes the observational error, which consists of DQ-1 measurement error, model error, and model
326 parameter error, defined as follows:

$$327 \quad y_p = \text{mean}\left(\int_{\text{time1}}^{\text{time2}} \text{ffXCO}_{2,p} dt\right), \quad y_a = \text{mean}\left(\int_{\text{time1}}^{\text{time2}} \text{ffXCO}_{2,a} dt\right) \quad 8$$

328 Here, $\text{ffXCO}_{2,p}$ represents the DQ-1 XCO₂ enhancement after removing the background concentration.
329 $\text{ffXCO}_{2,a}$ represents the simulated XCO₂ enhancement, obtained from the convolution of the fossil fuel
330 emission inventory and the footprint. We averaged the DQ-1 data over one-second intervals (3.35 km)
331 along the orbit to obtain $\text{ffXCO}_{2,p}$ and corresponding simulated data $\text{ffXCO}_{2,a}$.

332 According to the Bayesian inversion method, we transform the state vector into a scaling factor (λ), which
333 represents the constraint ability of pseudo-observations on regional emissions. The Jacobian matrix is
334 given by the simulated XCO₂ enhancement y_a . The observation error variance $\sigma_{\text{measurement}}^2$ and model
335 transport error variance σ_{mod}^2 are considered. We assume that DQ-1 observations are unbiased with respect
336 to the true values. Random errors were added to the observations, following a Gaussian distribution with
337 a standard deviation of 0.5 ppm, representing the lower limit of observational errors. The transport model
338 error was obtained by perturbing wind speed and wind direction errors; more wind observations help
339 reduce atmospheric transport uncertainties. For example, data assimilation systems have proven useful
340 in reducing atmospheric transport errors in data-rich areas like Los Angeles (Lauvaux et al., 2016).
341 Besides systematic wind direction errors, some areas exhibit positive/negative wind direction biases (Ye
342 et al., 2020). The X-STILT model proposed by Wu et al (Wu et al., 2021). can correct wind biases by
343 rotating model trajectories. the transport model error propagates by transforming the model ffXCO₂
344 plumes with added random wind speed and wind direction errors (by rotating ffXCO₂ plumes). To
345 estimate transport model uncertainty in the model ffXCO₂, we performed multiple (10^4 times) random
346 wind speed and direction perturbations on the model plume and extracted the uncertainty distribution of
347 ffXCO₂ using the 25th and 75th percentiles. We establish the loss function $J(x)$ to calculate the posterior



348 scaling factor:

$$349 \quad J(\lambda) = (y_p - y_a \lambda)^T S_p^{-1} (y_p - y_a \lambda) + (\lambda - \lambda_a)^2 \sigma_a^{-2} \quad 9$$

$$350 \quad \sigma_p^2 = \sigma_{\text{measurement}}^2 + \sigma_{\text{mod}}^2 \quad 10$$

351 Here, S_p represents the observational error covariance matrix. We assume that the observational errors of
 352 different orbits are uncorrelated, so S_p is a diagonal matrix with the observational error variances σ_p^2 on
 353 the main diagonal. Since the DQ-1 measurement errors and atmospheric transport model errors are
 354 unbiased and uncorrelated, we estimate σ_p^2 by summing both error variances. λ_a represents the prior value
 355 of the scaling factor, uniformly set to 1. σ_a represents the uncertainty of prior emissions, derived from
 356 previous studies combined with the emission characteristics of different cities. Since the ODIAC product
 357 does not provide uncertainty estimates, ODIAC was originally designed for atmospheric CO2 flux
 358 calculations to reduce model biases caused by coarse grid resolution. Considering the simple
 359 downscaling based on nightlights in ODIAC, urban emissions derived from ODIAC are affected by errors
 360 related to emission disaggregation. For example, (Lauvaux et al., 2016) reported a 20% difference
 361 compared to Gurney et al. (2012)(Kevin R Gurney et al., 2012) despite significant differences in emission
 362 modeling methods. Gurney et al. (2019)(Kevin R Gurney et al., 2019) further compared the ODIAC and
 363 Hestia products for four US cities (Los Angeles, Salt Lake City, Indianapolis, and Baltimore), finding
 364 city-wide emission differences ranging from -1.5% (Los Angeles) to 20.8% (Salt Lake City). Empirical
 365 values of ODIAC ffCO2 uncertainty can be obtained by comparing ODIAC inventories with other
 366 emission fluxes, such as high-resolution top-down satellite products. Smaller temporal scales result in
 367 greater empirical value deviations. Considering different city emission characteristics, such as industrial
 368 cities like Cairo and Riyadh with irregular emissions and large uncertainties in industrial emissions, we
 369 set prior emission uncertainties for these cities at 45%. For large cities with distinct and regular emission
 370 characteristics, the uncertainty is set at 25%, as their emission estimates are more accurate compared to
 371 industrial cities.

372 By minimizing the loss function, we obtain the posterior scaling factor $\hat{\lambda}$ and posterior uncertainty $\hat{\sigma}$:

$$373 \quad \hat{\lambda} = \lambda_a + \sigma_a^2 y_a^T (y_a S_p y_a^T + S_p)^{-1} (y_p - y_a \lambda_a) \quad 11$$

$$374 \quad \hat{\sigma}^2 = (y_a^T S_p^{-1} y_a + \sigma_a^{-2})^{-1} \quad 12$$



375 To evaluate the performance of the scaling factor, we define the mean kernel ($AK = \partial \hat{\lambda} / \partial \lambda$):

$$376 \quad AK = (y_a^T S_p^{-1} y_a + \sigma_a^{-2})^{-1} (y_a^T S_p^{-1} y_a) \quad 13$$

377 The value of AK closer to 1 indicates a more accurate estimation of the scaling factor.

378 2.5 OSSEs: Optimization of Emissions using Different DQ-1 Tracks

379 Given the limited number of DQ-1 overpass tracks and the impact of atmospheric conditions during
380 overpasses on emission optimization, we implemented Observing System Simulation Experiments
381 (OSSEs). These experiments were conducted using multiple DQ-1 tracks to constrain urban fossil fuel
382 emissions repeatedly and to statistically evaluate DQ-1's potential in constraining urban fossil fuel
383 emissions. Specifically, we initially screened all DQ-1 overpass tracks, selecting those located downwind
384 of major fossil fuel emission areas to better utilize DQ-1 data for constraining overall regional fossil fuel
385 emissions. For each city's overpass track, we extracted pseudo-observation data and modeling data.

386 DQ-1's advantage over other passive remote sensing satellites lies in its capability for nighttime
387 observations, which are largely unaffected by clouds and aerosols. Therefore, we studied the relationship
388 between daytime and nighttime observations and emission estimation uncertainties, as well as the impact
389 of different tracks and the number of tracks on emission estimates. We used the ODIAC fossil fuel
390 emission inventory as the prior emissions for the OSSEs, assuming that the prior emissions are the true
391 emissions and that emissions remain stable over a short period.

392 Pseudo-observation data and modeling data for each city were derived using the same method. Pseudo-
393 observation data were obtained by averaging the 1-second detection range of the selected DQ-1 overpass
394 tracks, with adjacent pseudo-observation data separated by 3.35 km (1 second). This method helps
395 eliminate some of the background noise and wind speed impacts on emission optimization. We assumed
396 that DQ-1 observations are unbiased with respect to the true values and added random errors to each DQ-
397 1 observation, with the error following a Gaussian distribution and a standard deviation of 0.5 ppm.
398 Pseudo-observation data are also unbiased relative to the true values, with random errors accumulated

399 over time for each observation data: $\sigma(l_s) = \sqrt{\frac{\sum_{i=1}^N \sigma_{i,DQ-1}^2}{N^2}}$ Here, N represents the random error of each
400 pseudo-observation data. Modeling data were obtained by convolving the emission inventory of the area
401 with the tracer contributions corresponding to the geographic locations.

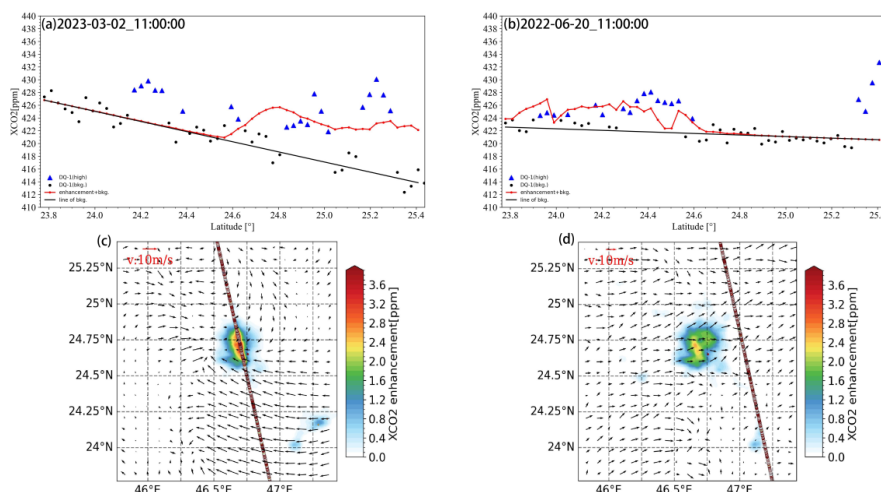


402 By using multiple DQ-1 overpass tracks to repeatedly constrain urban fossil fuel emissions and analyzing
403 the results statistically, we assessed the potential of DQ-1 in constraining fossil fuel emissions in urban
404 areas. This approach allowed us to examine the effectiveness of daytime and nighttime observations, the
405 influence of different overpass tracks, and the impact of track quantity on emission estimates.

406 **3 Results**

407 **3.1 Fossil Fuel Enhancement in Urban Areas**

408 In this section, we summarize the prior ffXCO₂ emissions for each study area. The total monthly
409 emissions for Beijing, Riyadh, and Cairo during the selected months are approximately 2.4-3.5 Mt
410 C/month, 2.3-3.3 Mt C/month, and 1.9-2.4 Mt C/month, respectively. We constrain emissions by
411 comparing observed and simulated ffXCO₂ enhancements. Here, ffXCO₂ enhancement is defined as the
412 increment in XCO₂ concentration caused by local fossil fuel emissions relative to the background XCO₂
413 level. The prior ffXCO₂ enhancement is simulated using the ODIAC prior emission inventory and the
414 STILT footprint convolution. The observed ffXCO₂ enhancement from DQ-1 is obtained by subtracting
415 the background concentration from the observational data (as detailed in Section 2.3.3 and shown in
416 Figure 3). By comparing the prior ffXCO₂ enhancement with the observed ffXCO₂ enhancement, we
417 evaluate the trends in ffXCO₂ changes along the tracks and explore the sources and detection capabilities
418 of the ffXCO₂ signal.



419

420 **Figure 3: Comparison of the simulated and observed fFXCO₂ enhancements from DQ-1 data over Riyadh**
 421 **on March 02, 2023 and June 20, 2022 around 11:00 UTC. Figures (a) and (b) show the DQ-1 XCO₂ (black**
 422 **dots and blue triangles) and the simulated XCO₂ (red solid line, sum of simulated fFXCO₂ and background**
 423 **concentrations) along the two orbits, averaged over 1 s. The black dots represent the background**
 424 **concentrations involved in deriving the background. The black dots represent the data involved in the**
 425 **derivation of the background concentration (black solid line), which are linearly regressed against latitude**
 426 **after a discrete wavelet transform. Figures (c) and (d) show the simulated fFXCO₂ and the observed fFXCO₂**
 427 **obtained from the DQ-1 data, background XCO₂ concentrations have been subtracted. Vectors represent 10**
 428 **m wind speeds and reference vectors represent 10 m/s wind speeds.**

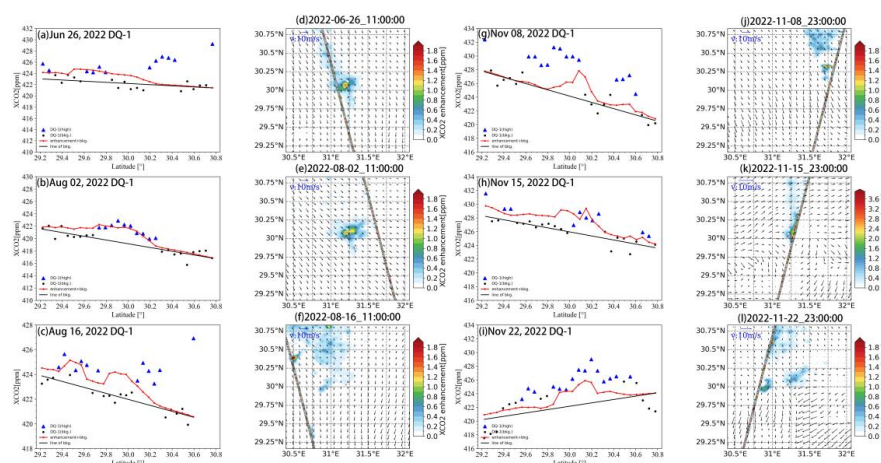
429 Figure 3 presents the results of two DQ-1 overpasses over Riyadh on March 2, 2023, and June 20, 2022,
 430 at 11:00 AM. Figures 3a and 3b show the simulated and observed fFXCO₂ enhancements as a function
 431 of latitude for these two overpasses. The maximum fFXCO₂ enhancements observed along the two tracks
 432 were 8 ppm and 5 ppm, respectively.

433 In the overpass on March 2, significant fFXCO₂ enhancements were observed by DQ-1 between 24.8°N
 434 and 25.3°N, with the simulated fFXCO₂ also responding to this enhancement. Although the peak
 435 observed values were narrower than the simulated values, both were of similar magnitudes, with only
 436 slight differences, and their trends were largely consistent. However, the simulated fFXCO₂ did not
 437 respond to the observed enhancement in the 24.1°N to 24.3°N range, which may be due to the sensitivity
 438 of the STILT footprint to wind direction.

439 In the overpass on June 20, the agreement between the simulated and observed values was better than in
 440 the March 2 overpass. The observed peak and the simulated peak were both within the 23.8°N to 24.6°N
 441 range, with a difference of less than 1 ppm. The differences between the results of the two tracks may be



442 because the March 2 track passed through the city's main emission area and intersected the simulated
 443 plume (Figure 3c). In this case, ffXCO₂ fluctuations were minimal, with values remaining high relative
 444 to the background concentration, making it difficult to detect significant enhancements. In contrast, the
 445 June 20 track was downwind of the main emission area, making it more sensitive to the city's fossil fuel
 446 emissions and resulting in better agreement between the simulated and observed values.



447 **Figure 4:** Similar to Fig. 3, but for the trajectories of DQ-1 over Cairo on June 26 (a and d), August 02 (b and
 448 e), August 16 (c and f) at 11:00 UTC, November 08 (g and j), and November 15 (h and k) at about 23:00 UTC
 449 in 2022.
 450

451 For Cairo, we examined ffXCO₂ enhancements using six DQ-1 overpasses on July 26, August 2, August
 452 16, November 8, November 15, and November 22, 2022 (Figure 4). Compared to Riyadh, the simulated
 453 ffXCO₂ enhancements over Cairo were mostly below 2 ppm, indicating lower overall emissions in Cairo
 454 than in Riyadh. The simulated ffXCO₂ enhancements over Cairo were more dispersed, showing a multi-
 455 point distribution rather than the concentrated enhancements observed over Riyadh.

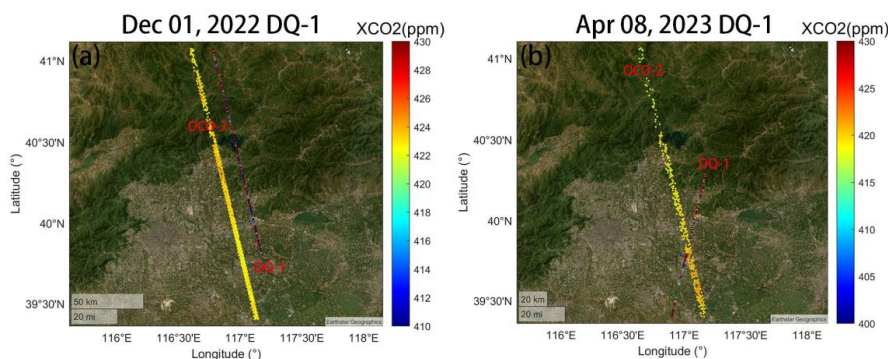
456 The observed ffXCO₂ enhancements over Cairo were generally higher and narrower than the simulated
 457 ones, which were smoother. Despite these differences, the trends in ffXCO₂ enhancements between the
 458 simulations and observations were similar and of the same magnitude, except for the July 26 simulation,
 459 which overlooked some observed enhancements between 30.2°N and 30.4°N, and the November 8
 460 overpass, where a spatial shift of approximately 0.2° was observed between the simulated and observed
 461 ffXCO₂ enhancements.

462 Overall, the comparison between DQ-1 observations and WRF-STILT-based simulations suggests that



463 the DQ-1 satellite is well-suited for fine-scale urban emission optimization. This indicates that DQ-1 can
464 effectively be used for detailed monitoring and analysis of urban emissions.

465 3.2 Comparison of DQ-1 and OCO-2 Restraint Capabilities



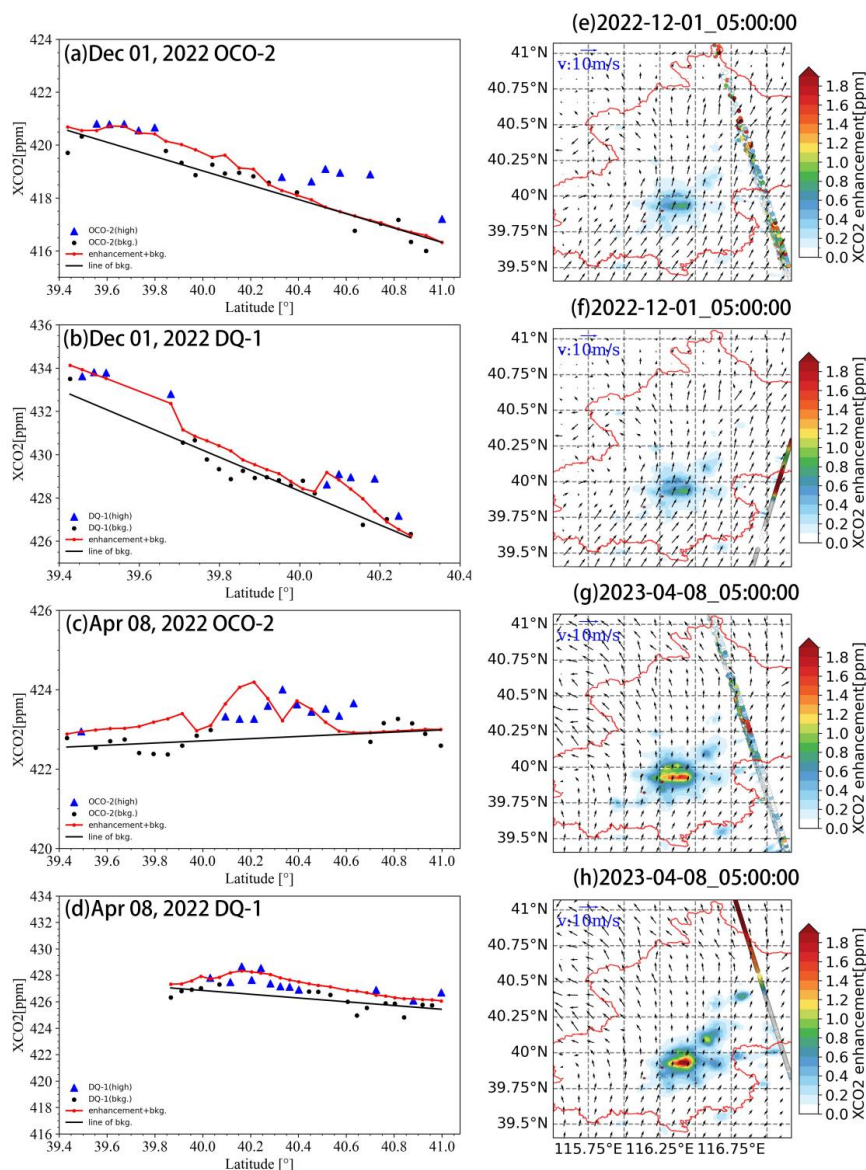
466
467 **Figure 5: (a) and (b) show the position and XCO₂ data of two pairs of OCO-2 and DQ-1 orbits that we selected**
468 **for transit to Beijing at 05:00 on December 01, 2022 and 05:00 on April 08, 2023, respectively**

469 Considering previous studies that used OCO-2/3 and GOSAT for inversion (Patra et al., 2021; Roten et
470 al., 2022; H. Wang et al., 2019), we selected one of these inversion methods (Ye et al., 2020) for
471 comparison with DQ-1 inversions and validation using TCCON site data. The posterior scaling factor
472 was applied to the ODIAC inventory flux to simulate XCO₂ at TCCON site locations, and these
473 simulations were compared with TCCON data, assumed to be the true XCO₂ at those locations. The
474 simulated XCO₂ for TCCON was obtained using an integration method provided by TCCON, with 51
475 altitude levels corresponding to the input levels of our STILT model. The footprints from these 51 altitude
476 levels were integrated using the integration operator `integration_operator_x2019` and the averaging
477 kernel `ak_xco2` to obtain the simulated XCO₂.

478 To better compare the inversion results from OCO-2 and DQ-1, we selected tracks that were spatially
479 and temporally close and located downwind of major urban emission areas. Figure 5 shows two pairs of
480 OCO-2 and DQ-1 tracks over Beijing on December 1, 2022, and April 8, 2023, both at 05:00, passing
481 through the major emission downwind area of the city. The figure shows ffXCO_2 enhancements and
482 wind fields at the time of the satellite overpasses. The results clearly indicate significant ffXCO_2
483 enhancements, exceeding 2 ppm in April, demonstrating that DQ-1 can observe notable ffXCO_2
484 enhancements from space.



485 Figures 5e-h show that the ffXCO_2 enhancements simulated from DQ-1 and OCO-2 overpasses are of
486 similar magnitude and spatial distribution, with strong spatial consistency across different times due to
487 stable local emissions and wind fields. Beijing's topography, with high elevations in the northwest and
488 low-lying plains in the southeast, influences the prevailing west-to-east winds, and the flat terrain of the
489 main urban area means the simulated ffXCO_2 is minimally affected by topography. The smaller ffXCO_2
490 enhancements observed on December 1 compared to April 8 are primarily due to wind directions
491 affecting the track within the 40.2° - 41° range, making it difficult to simulate emissions.
492 This comparison highlights the capability of DQ-1 to effectively observe and simulate urban ffXCO_2
493 enhancements, supporting its application in fine-scale emission optimization.



494

495 **Figure 6:** Similar to Fig. 3, (a)-(d) show the simulated ffXCO₂ and measured ffXCO₂ for the DQ-1 and OCO-
 496 2 orbits transiting Beijing at 05:00 UTC 01 December 2022 and 05:00 UTC 08 April 2023, and (e)-(h) represent
 497 the comparison of the simulated ffXCO₂ (colored shadows) with the observed ffXCO₂ enhancement (colored
 498 dots, minus background concentrations) from DQ-1 data collected over Beijing at ~05:00 UTC. Each panel is
 499 labeled with the date of observation. Vectors represent 10 m wind speeds and reference vectors represent 10
 500 m/s wind speeds.

501 Figure 6 (a-d) illustrates the simulated and observed XCO₂ for two pairs of DQ-1 and OCO-2 tracks.

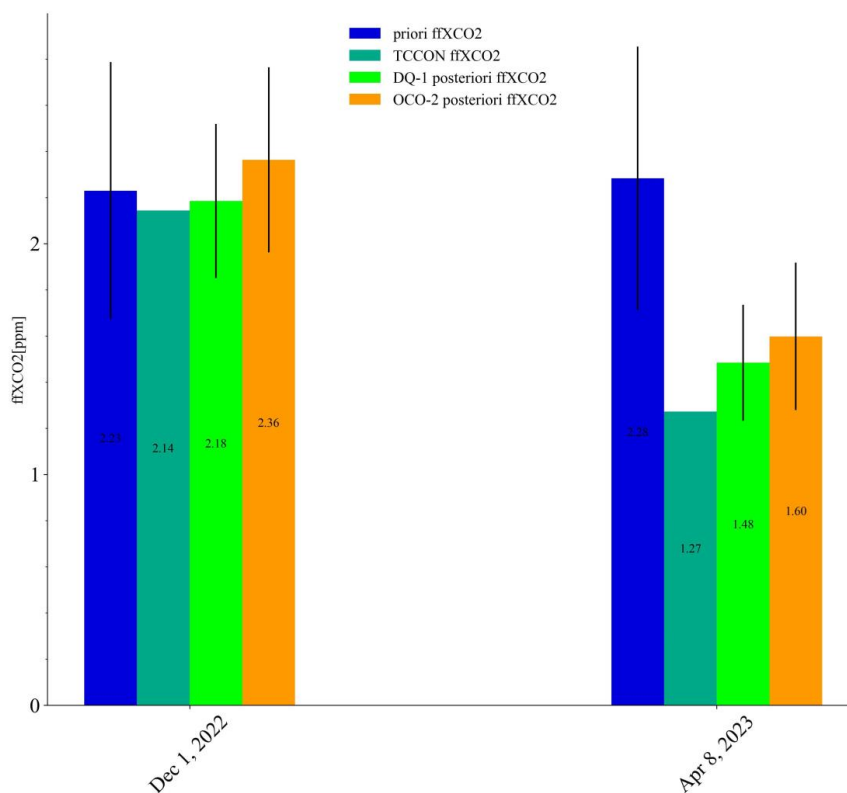


502 The simulated XCO₂ (red line in the figures) is derived by adding the background concentration to the
503 simulated ffXCO₂ extracted along the satellite tracks. Overall, both OCO-2 and DQ-1 observations
504 exhibit similar distributions, with high-value points located in the same latitude ranges. DQ-1
505 observations are generally 4-8 ppm higher than OCO-2, attributed to the inherent characteristics of the
506 satellites—DQ-1 being an active lidar satellite, largely unaffected by clouds and aerosols. This systematic
507 difference can be mitigated during background concentration extraction due to the overall similarity in
508 data distribution.

509 On December 1 and April 8, DQ-1 and OCO-2 observed ffXCO₂ enhancements of approximately ~2.5
510 ppm and ~1.5 ppm, respectively. Although OCO-2 did not capture the ffXCO₂ enhancement within the
511 40.2°-41° range on December 1, and there was a ~0.15° spatial shift between observed and simulated
512 XCO₂ peaks on April 8, the simulated ffXCO₂ was of the same magnitude as the observations. This
513 indicates that DQ-1 performs comparably to OCO-2 in urban-scale inversions. The peak shift in OCO-2
514 data might be due to errors in the horizontal wind field. The background gradient on December 1 was
515 more pronounced than on April 8, and the integrated ffXCO₂ enhancement along the track was consistent
516 with DQ-1 measurements, validating the latitude gradient-based background extraction method for
517 urban-scale inversions.

518 Figure 7 compares TCCON site observations within the Beijing study area with the simulated results for
519 December 1 and April 8. The prior ffXCO₂ (blue bars) represents the simulated ffXCO₂ at the TCCON
520 site, obtained using the previously described simulation method. The posterior ffXCO₂ (light green and
521 orange bars) is derived by applying the posterior scaling factors from DQ-1 and OCO-2 overpass tracks
522 to the prior ffXCO₂, with posterior uncertainties indicated. The true value, provided by TCCON products,
523 is shown by the dark green bars.

524 Overall, DQ-1 and OCO-2 inversion results are similar in magnitude, with DQ-1 results closer to TCCON
525 observations. The differences between DQ-1 results and TCCON observations are 0.9% and 16% for
526 December 1 and April 8, respectively, compared to 10% and 25% for OCO-2. This demonstrates that
527 DQ-1 can effectively constrain urban fossil fuel emissions, performing comparably to, or even surpassing,
528 OCO-2 in certain tracks.

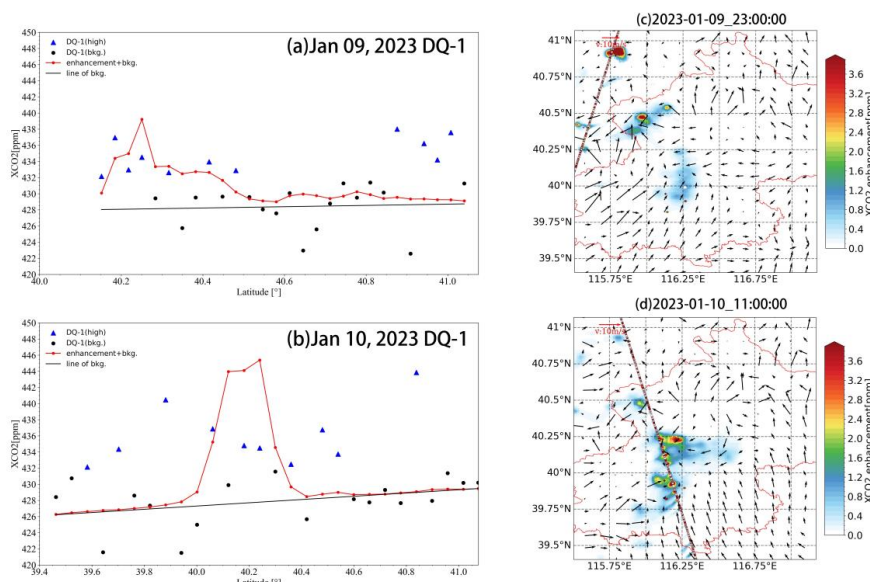


529

530 **Figure 7: TCCON site simulations received fXCO₂ (blue columns represent simulations using a priori**
531 **ODIAC lists, bright green columns represent simulations using a posteriori lists estimated with DQ-1, orange**
532 **columns represent simulations using a posteriori lists estimated with OCO-2, and dark green columns**
533 **represent fXCO₂ observed by TCCON). The black lines on the columns represent uncertainties.**



534 **3.3 Impact of DQ-1 in Estimating Biotic Fluxes using Daytime vs. Nighttime Tracks**



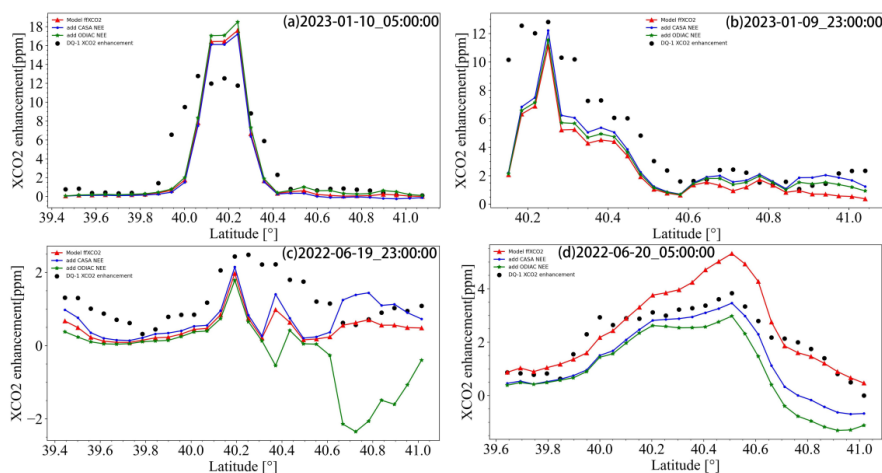
535
536 **Figure 8: Orbital simulation results for a pair of diurnal observations of the transit of Beijing on January 09,**
537 **2023 at about 23:00 (night) and January 10, 2023 at about 11:00 (day) UTC.**

538 Both biosphere carbon flux and fossil fuel emissions influence XCO₂ variations. This section examines
539 the impact of biosphere flux on emission estimates. When ffXCO₂ significantly exceeds biosphere
540 carbon flux, the biosphere's contribution to XCO₂ changes can be negligible (e.g., in Cairo and Riyadh,
541 where the spatial gradient of NEE is much smaller than fossil fuel emissions). This study attributes
542 biosphere carbon flux to vegetation production and human emissions. This part of carbon emissions
543 varies with the day-night cycle. During the day, vegetation absorbs CO₂ through photosynthesis, which
544 significantly outweighs CO₂ release through respiration. At night, vegetation only undergoes respiration,
545 releasing CO₂.

546 As the world's first lidar satellite capable of observing XCO₂ at night, DQ-1 offers groundbreaking
547 potential in studying diurnal variations in urban emissions. This section leverages this feature to observe
548 the impact of vegetation rhythm and human activities on XCO₂ changes. We compare global three-hourly
549 CASA data and ten-day average NEE data from ODIAC. ODIAC's ten-day average data cannot separate
550 diurnal NEE variations, while the higher temporal resolution of CASA can effectively capture the time
551 gradient of NEE within the same day. We will illustrate the impact of NEE on inversion and how this



552 impact changes between day and night. Previous satellite-based urban flux inversions lacked night-time
553 data, preventing day-night comparisons and separation of nocturnal and diurnal CO₂ emissions.
554 For this study, we selected two tracks on January 9, 2023, at 23:00 and January 10, 2023, at 11:00 (UTC).
555 Given the close timing of these tracks, we assume the total fossil fuel emissions are the same for both.
556 The January 9 track is approximately 0.5° (about 50 km) downwind from the main urban emissions, with
557 an average wind speed greater than 3 m/s. Thus, the emissions detected by this track are considered to
558 originate from the previous five hours. The January 10 track passes through the main urban emission
559 area, capturing emissions effectively. We simulate forward eight-hour gas diffusion (sunset on January 9
560 at 09:00 and sunrise on January 10 at 15:35 UTC). The simulated enhancement for the January 9 track is
561 assumed to come entirely from night-time emissions, while the January 10 enhancement comes from
562 daytime emissions. Comparing the simulation results with observations, both are of the same magnitude,
563 indicating that the forward eight-hour simulation effectively captures the observed ffXCO₂ enhancement.
564 To explore the impact of diurnal biosphere carbon flux on XCO₂ enhancement, we couple prior emissions
565 from ODIAAC with spatially scaled NEE data as the new prior emissions, then simulate the track XCO₂.
566 Using constant boundary conditions, latitude changes do not need to be considered for background
567 concentration. Therefore, local XCO₂ enhancement is defined as the total XCO₂ minus the minimum
568 XCO₂ value in the track. The XCO₂ enhancement measured by DQ-1 is derived using methods outlined
569 in previous sections.
570 This approach allows us to accurately account for both daytime and nighttime variations in XCO₂ due
571 to biosphere activity, providing a comprehensive view of the urban carbon flux.



572

573 **Figure 9: (a)-(d) represent the contribution of orbital XCO₂ enhancement and biospheric fluxes to the local**
 574 **XCO₂ enhancement for two pairs of diurnal observations on 09 and 10 January 2023 and 19 and 20 June**
 575 **2022, the black dots represent the 1-second averaged observations (subtracted from the background values)**
 576 **on each orbit, the red solid line represents the simulated fXCO₂, and the green and blue solid lines represent**
 577 **the simulated ΔXCO₂ (fossil fuel and biosphere fluxes) using different NEE data for simulated ΔXCO₂ (fossil**
 578 **fuel and biogenic fluxes), where the green line uses ten-day averaged ODIAC NEE data and the blue line uses**
 579 **CASA three-hourly NEE data.**

580 Figure 9 presents a comparison of simulated and observed XCO₂ enhancements for two pairs of day and
 581 night overpass tracks over Beijing on January 9, 2023, at 23:00, January 10 at 05:00, June 19, 2022, at
 582 23:00, and June 20 at 05:00. Overall, the simulated XCO₂ enhancements (including the biosphere XCO₂
 583 signal) align more closely with the observed ΔXCO₂ (black dots) than the simulated fXCO₂ alone (red
 584 line).

585 The figure shows that the XCO₂ enhancements using CASA's diurnal NEE data differ significantly from
 586 those using ODIAC's ten-day average NEE data. The simulation for the June 19 track at 23:00 indicates
 587 that using CASA's night-time NEE data (blue line) can accurately simulate the observed XCO₂
 588 enhancement, coming closer to the observed XCO₂ enhancement than the fXCO₂ simulation alone. In
 589 contrast, the simulation using ODIAC's ten-day average NEE data (green line) shows a notable CO₂
 590 absorption phenomenon in the 40.2°-41° range, starkly different from the CASA results and the observed
 591 XCO₂ enhancement. This discrepancy arises because ODIAC's ten-day average NEE data are insensitive
 592 to short-term temporal variations and cannot reflect diurnal changes within a day. Moreover, this period
 593 is Beijing's summer, with vigorous daytime vegetation activity leading to CO₂ absorption and a



594 consequent drop in XCO₂ (as seen in Figure 9d, where the daytime simulated XCO₂ enhancement is
 595 much lower than fXCO₂). According to the June 19 simulation results, biosphere flux-induced XCO₂
 596 changes account for 21.2% (CASA) and -54.3% (ODIAC) of the observed XCO₂ enhancement.
 597 For the January 9 track at 23:00, both CASA and ODIAC data show significant XCO₂ enhancements.
 598 However, the CASA simulation aligns more closely with the observations. This difference may be
 599 because ODIAC's ten-day average data, influenced by daytime data, diminish its accuracy in night-time
 600 scenarios. The simulation results for the January 9 track show that biosphere flux-induced local XCO₂
 601 enhancements account for 13.37% (CASA) and 7.73% (ODIAC) of the observed comprehensive XCO₂
 602 enhancement.
 603 Overall, the biosphere flux's impact on XCO₂ enhancement varies significantly between day and night.
 604 In urban-scale inversions, DQ-1's ability to rapidly revisit both day and night can further optimize the
 605 influence of biosphere flux on inversion accuracy. This capability highlights DQ-1's potential to provide
 606 more precise urban-scale fossil fuel emission constraints, especially by distinguishing diurnal variations
 607 in biosphere activity.

608 3.4 Emission Estimates and a Posteriori Uncertainties

609 **Table 1 Results of inversion of urban emission scaling factors for selected cities using DQ-1 XCO₂ data**

City	Overpass	Prior total emission (Mt C/month)	Prior total	Measurement	Transport model	Scaling factor(λ) \pm posterior uncertainty ($\hat{\sigma}$)
			emission uncertainty (σ_e)	uncertainty ($\sigma_{measurement}$)	uncertainty (σ_{Model} , units: ppm)	
Riyadh	02 March 2023	2.37	45%	1.03	2.53	0.75 ± 0.20
	20 June 2022	3.49		0.98	2.58	0.86 ± 0.16
Beijing	01 December 2022	4.61	25%	1.88/ 2.11	2.64	0.98 ± 0.15 1.09 ± 0.18
	08 April 2023	3.35		1.57/ 1.93	1.79	0.65 ± 0.11 0.70 ± 0.14
	09 January 2023	2.40		2.01	3.04	0.91 ± 0.12
	10 January 2023	2.40		1.99	1.45	1.00 ± 0.14
	19 June 2022	3.81		1.78	2.11	0.96 ± 0.16
	20 June 2022	3.81		1.52	1.12	0.53 ± 0.11



Cairo	26 June 2022	2.43	45%	1.08	0.56	1.06 ± 0.20
	02 August 2022	2.49		1.45	0.71	0.98 ± 0.12
	16 August 2022	2.49		1.67	0.87	1.21 ± 0.14
	08 November 2022	1.96		1.22	0.36	1.15 ± 0.16
	15 November 2022	1.96		0.98	1.31	1.19 ± 0.11
	22 November 2022	1.96		1.11	0.21	1.06 ± 0.13

610 **Notes. Scaling factors and their a posteriori uncertainties are shown for each orbit, as well as integrated**
 611 **information for all selected orbits. Uncertainty components are listed for each orbit, including the a**
 612 **priori uncertainty in the scaling factor and the measurement and transport uncertainty in the integral**
 613 **ffXCO₂ (some selected orbital data inverted using OCO-2 data are bolded).**

614 In this section, we present the inversion estimation results for emissions from Riyadh, Cairo, and Beijing
 615 using the DQ-1 tracks shown in Section 3.1. The inversion process considers uncertainties arising from
 616 both measurement and transport. The inversion yields a scaling factor for the total emissions for each
 617 selected city. Specifically, for Beijing, we compare the inversion results with the simultaneously passing
 618 OCO-2 tracks.

619 Each selected track underwent inversion. The table below shows the posterior emission scaling factors
 620 for each track, along with the uncertainties in the measured and simulated ffXCO₂. These uncertainties
 621 were determined using the methods described in Section 2.4. Notably, the prior uncertainty in the
 622 emission scaling factors for Beijing was set at 25%, compared to Riyadh and Cairo, reflecting better
 623 knowledge of emissions from such a world-class megacity (see Section 2.4.2).

624 For the selected tracks over Riyadh, Cairo, and Beijing, the posterior scaling factors were 0.75-0.86,
 625 0.98-1.21, and 0.53-1.06, respectively (Table 1). The posterior emission scaling factors exhibit significant
 626 temporal variability, influenced by background conditions. As described in the previous section, the
 627 emissions detected by the track depend on its distance from the major emission regions and the domain-
 628 averaged wind speed at the time. The domain-averaged wind speed for the selected tracks was
 629 consistently above 3 m/s. Based on meteorological conditions, the posterior values represent estimates
 630 of city emissions for the hours preceding the overpass time. The posterior uncertainty in the emission
 631 scaling factors was 0.16-0.20 for Riyadh, 0.11-0.20 for Cairo, and 0.11-0.16 for Beijing. Compared to
 632 Beijing, the posterior scaling factor uncertainties were generally higher for Riyadh and Cairo.



633 As discussed in Section 2.4, the prior emission uncertainties were set to reflect measurement and
634 transport errors. Table 1 shows that the relative contributions of observation error and transport error vary
635 across the three cities. For Riyadh, the transport error was significantly larger than the observation error,
636 while for Cairo, the transport error was much smaller than the observation error. In Beijing, the relative
637 sizes of transport error and observation error varied. The posterior scaling factors for Beijing's two OCO-
638 2 tracks were almost identical to those from DQ-1, with higher posterior uncertainty due to higher
639 observation error. Overall, Beijing's posterior uncertainty was lower than that of Cairo and Riyadh,
640 attributable to more stable prior emission characteristics.

641 Previous research (Ye et al., 2020) highlighted that the scarcity of OCO-2 tracks near many cities remains
642 a major limitation in regularly quantifying emissions and objectively tracking temporal variations from
643 space. In contrast, DQ-1's minimal sensitivity to clouds and aerosols allows for more tracks available for
644 inversion. Our experiments in Beijing, Cairo, and Riyadh found that, on average, more than six tracks
645 per month were available for inversion, including day and night overpasses on the same day, further
646 constraining city emissions (see Section 3.3).

647 Based on the results in Table 1, we averaged the posterior emission scaling factors and uncertainties for
648 each city's tracks, yielding mean scaling factors and uncertainties of 0.80 ± 0.18 for Riyadh, 1.10 ± 0.14 for
649 Cairo, and 0.83 ± 0.13 for Beijing. This indicates that, for the periods represented by the observations, the
650 prior monthly ODIAC product overestimates emissions for Beijing and Riyadh, while underestimating
651 emissions for Cairo.

652 **4 Discussion**

653 **4.1 Atmospheric Transport Model Errors**

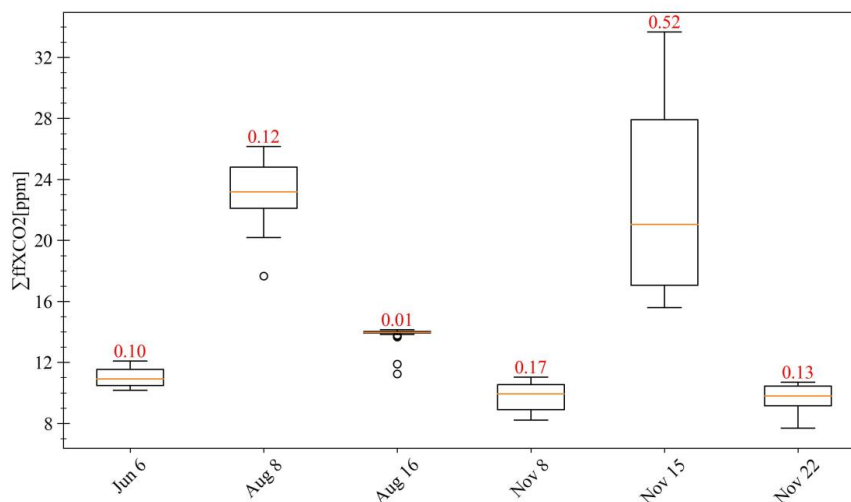
654 Systematic errors in model transport and erroneous statistical assumptions can significantly diminish the
655 improvements in land-based uncertainty by approximately a factor of two (J. Wang et al., 2014). Hence,
656 it is essential to control systematic errors and inaccuracies in transport models while minimizing random
657 errors in DQ-1 observations. In Observing System Simulation Experiments (OSSEs), we assess the
658 potential impacts of observational and transport errors on the entire inversion process. Transport errors
659 of tracers in the atmosphere can lead to inaccuracies in flux estimates derived from concentration



660 observations. Typically, "inversion" methods either ignore transport errors or only provide a rough
661 evaluation of their impact (J. Lin & Gerbig, 2005). This section focuses on how uncertainties in
662 atmospheric transport model outputs influence CO₂ flux inversion.

663 In our experiments, we set the prior flux uncertainty to 25%-40% based on the emission characteristics
664 of different cities. The uncertainty in DQ-1 XCO₂ observations was fixed at 0.5 ppm, representing the
665 lower limit of observational error. We examined the effects of wind speed and direction errors on the
666 performance of the inversion method. The errors in the transport model were propagated by treating them
667 as conversions of model ffXCO₂ plumes. Notably, for the cities studied, errors were assumed to be
668 unbiased. Wind direction errors were analyzed by rotating the plumes around the emission center and
669 incorporating random wind speed errors.

670 We illustrate these concepts using six tracks over Cairo. The overall ffXCO₂ distribution was generated
671 by applying random positive and negative wind direction biases ($>-10^\circ$, $<10^\circ$) to each track's STILT
672 footprint, rotating it 10^4 times, and adding positive/negative wind speed biases (>-1 m/s, <1 m/s). Overall,
673 the temporal variability in the posterior emission scaling factors and uncertainties can be attributed to
674 transport model errors. The transport model error significantly influenced the observed ffXCO₂
675 distribution. Specifically, the track on November 15 was most affected by transport model errors, likely
676 due to its passage through the plume boundary. In contrast, the track on August 16 experienced minimal
677 transport model errors, as it was further from the simulated ffXCO₂ plume, making it less sensitive to
678 small wind direction and speed errors.



679

680 **Figure 10:** Box plots of the modeled integral fXCO₂ enhancement (Σ fXCO₂, m) for selected OCO-2 orbits
681 over Cairo at the date labeled on the x-axis (2022). For each box, the center line indicates the median (q₂),
682 and the bottom and top edges of the box indicate the 25th and 75th percentiles (q₁ and q₃), respectively. The
683 whiskers extend to the maximum and minimum values. The numbers are the ratio of the interquartile spacing
684 (q₃ - q₁) to the median (q₂).

685 4.2 The Challenge of Separating Biological Fluxes in Day and Night Orbits

686 In Section 3.3, we detailed how DQ-1's short-term day-night revisit capability allows for the
687 consideration of diurnal and nocturnal biogenic fluxes in emission inversions. Typically, large-scale
688 inversions do not account for uncertainties in fossil fuel emission inventories and treat biogenic fluxes
689 as uncertainties in prior fluxes (J. Wang et al., 2014). Studies focused on urban-scale inversions that do
690 not utilize nocturnal tracks, while directly considering biogenic flux impacts, have not accounted for the
691 diurnal variation of biogenic fluxes (Ye et al., 2020). In this study, we leveraged DQ-1's nocturnal
692 observations to provide a method for separately considering biogenic flux effects during day and night.
693 Our results indicate that using daytime average NEE data and nighttime NEE data can result in
694 differences of up to 70% in inversion outcomes.

695 However, this approach has limitations in large-scale inversions. Separating daytime and nighttime
696 emissions necessitates a limited transport time due to the constraints of the transport model, which means
697 that simulated particles cannot travel long distances under limited wind speed and time conditions. To
698 address this, more frequent overpass tracks, including those from geostationary carbon cycle observation



699 satellites such as GeoCarb (Moore III et al., 2018), Total Carbon Column Observing Network
700 (TCCON)(Toon et al., 2009), and MicroCARB, could enhance large-scale day-night cross-observations
701 and support separate daytime and nighttime inversions. Currently, the number of DQ-1 tracks does not
702 support large-scale separate day-night inversions. In large-scale flux inversions, biogenic fluxes are
703 typically used as prior uncertainty over weekly or monthly periods. Such long-term and wide-scale data
704 assimilation reduces the impact of diurnal biogenic flux variations on inversion results. Unlike other
705 satellite measurements that are restricted to daytime clear-sky conditions, DQ-1's XCO₂ measurements
706 provide uniform temporal sampling, thus allowing effective quantification of diurnal variations in
707 emissions.

708 Accurate downscaling methods for biogenic fluxes, such as the Solar-Induced Fluorescence Model
709 (SMUrF) (Wu et al., 2021), and advanced vegetation models, like the Vegetation Photosynthesis and
710 Respiration Model (VPRM) (Luo et al., 2022; Mahadevan et al., 2008) are crucial for precise biogenic
711 flux calculations. Radiocarbon and land surface solar-induced fluorescence (SIF) data aid in
712 distinguishing between fossil fuel CO₂ and biogenic CO₂ (Fischer et al., 2017). Recent research indicates
713 that SIF serves as a better indicator or proxy for gross or net primary production compared to other
714 vegetation indices.

715 **4.3 Insights From Results of the OSSEs**

716 In the emission inversion process, prior emissions are considered as fully distributed, optimizing regional
717 emissions for an entire city using a scaling factor, in contrast to grid-specific inversions. As noted by
718 previous research, using a single scaling factor for the entire city limits the flexibility to capture true
719 spatial variations in fluxes compared to grid-specific inversions. Estimating prior emission uncertainties
720 at the grid scale is challenging because grid-scale emission uncertainties are typically much larger than
721 those using scaling factors (Andres et al., 2012).

722 Apart from uncertainties in the transport model, DQ-1 measurements, and biogenic fluxes, several
723 additional error sources may introduce biases in the inversion results. DQ-1 data's measurement errors
724 are assumed to be spatially uncorrelated due to the lack of high-resolution correlation data. Additionally,
725 random components of nonlinear and interference errors in retrievals may introduce significant errors in
726 the inversions (Connor et al., 2016). In our OSSE, measurement uncertainty is assessed at its lower bound.



727 Simulation results for Riyadh and Beijing indicate that the enhancement of ffXCO_2 generally exceeds
728 1.5 ppm and can reach up to approximately 5 ppm, surpassing the uncertainties in land-based
729 observations (around 1 ppm) (Annmarie Eldering et al., 2017). In contrast, Cairo's ffXCO_2 values are
730 mostly below 2.0 ppm, with some hotspots near high-emission industries such as power plants. Detecting
731 CO_2 plumes in smaller cities is challenging due to limited detectability of fossil fuel-derived CO_2 plumes.
732 Factors limiting detectability include: 1) The number and location of overpass tracks. 2) Overlap
733 enhancements from nearby cities or point sources. 3) Low ffCO_2 emissions. To improve the detection of
734 city plumes, more ground-based in situ measurements and high-altitude satellites with enhanced
735 detection capabilities are necessary.

736 **5 Conclusions**

737 This study presents the use of DQ-1's XCO_2 observation data to constrain fossil fuel emissions in various
738 urban regions and evaluates its capabilities. By coupling WRF and STILT, a high-resolution forward
739 transport model was developed to simulate and illustrate the structure and details of urban-scale fossil
740 fuel XCO_2 plumes and assess the relationship between simulated and observed XCO_2 . Throughout the
741 inversion process, we considered DQ-1's observational errors, transport model errors, and the impact of
742 DQ-1's day-night observation capability on assessing the temporal variation of biosphere fluxes in urban
743 emissions. Employing a Bayesian inversion approach, we optimized CO_2 emissions from fossil fuels in
744 Beijing, Riyadh, and Cairo using DQ-1 data collected from March to December 2022, focusing on
745 downwind tracks in major urban emission areas where significant XCO_2 enhancements were detected.
746 Pseudo-data experiments, based on high-resolution forward simulations from real cases, were conducted
747 to evaluate the potential of using multiple DQ-1 tracks while considering measurement and transport
748 model errors. Our results showed that the posterior scaling factors for the three cities ranged from 0.53
749 to 1.06, 0.75 to 0.86, and 0.98 to 1.21, respectively, with Riyadh exhibiting the highest posterior
750 uncertainty. Notably, some simulations revealed that posterior scaling factor uncertainties are influenced
751 by the relative position of tracks to plumes and positive or negative wind direction biases in the region.
752 Our assessment of spatial and temporal gradients in biosphere fluxes revealed that, at certain times in
753 Beijing, despite significant ffCO_2 emissions, a notable portion of the local XCO_2 enhancement (20%
754 and 13%, respectively) was attributable to local biosphere fluxes. This could lead to an overestimation



755 of total emissions by approximately $33\% \pm 20\%$ and $13 \pm 7\%$. By incorporating CASA and ODIAC
756 biosphere flux data and examining day-night crossing tracks on the same day, we found that separately
757 considering day and night biosphere fluxes can improve the accuracy of local XCO₂ enhancement
758 calculations by 30%-70% compared to using daily average biosphere fluxes. This indicates that
759 leveraging the short-term, rapid day-night crossing capability of DQ-1, along with more accurate
760 biosphere flux estimation models, has the potential to reduce uncertainties in emission estimates due to
761 biosphere fluxes.

762 For biosphere flux cities with similar total CO₂ emissions but lower fossil fuel emissions, the contribution
763 of biosphere fluxes is expected to be higher than indicated. Therefore, for cities in mid-latitude and
764 equatorial regions with significant local and regional biosphere fluxes, accurately interpreting XCO₂
765 detection results is crucial. Future improvements in constraining urban fossil fuel CO₂ emissions using
766 DQ-1 data or other polar orbit measurements should consider the temporal and spatial correlations of
767 previous emission errors, which were not included in this inversion.

768 For applying these methods to larger-scale flux inversions, advanced satellites with shorter revisit cycles
769 and denser ground-based stations are essential. Additionally, optimizing city emission scaling factors
770 requires more information on prior emission uncertainties to better understand spatial and temporal
771 characteristics of urban-scale emissions. The appropriate number of constraints for urban emissions will
772 depend on the spatial and temporal resolution of target city emissions and the precision required to
773 support policy decisions. Our results demonstrate that DQ-1 or similar missions have significant potential
774 to constrain overall emissions from cities with intensified fossil fuel emissions, and utilizing DQ-1's
775 unique day-night crossing capability, we can establish frameworks for rapid day-night flux inversions at
776 the urban scale. This will further elucidate the spatial and temporal structure of biosphere flux
777 contributions to urban emissions and provide valuable insights for policy-making. We anticipate that DQ-
778 1 data will effectively enhance the accuracy and precision of urban fossil fuel carbon flux estimates, in
779 conjunction with observations from other platforms to support emission reduction strategies.

780 **Competing interests**

781 The contact author has declared that none of the authors has any competing interests



782 **References**

- 783 Abshire, J. B., Ramanathan, A., Riris, H., Allan, G. R., Sun, X., Hasselbrack, W. E., . . . DiGangi, J.
784 (2017). Airborne Measurements of CO₂ Column Concentrations made with a Pulsed IPDA
785 Lidar using a Multiple-Wavelength-Locked Laser and HgCdTe APD Detector. *Atmos. Meas.*
786 *Tech. Discuss.*, 2017, 1-36. doi:10.5194/amt-2017-360
- 787 Amediek, A., Fix, A., Wirth, M., & Ehret, G. (2008). Development of an OPO system at 1.57 μm for
788 integrated path DIAL measurement of atmospheric carbon dioxide. *Applied Physics B*, 92(2),
789 295-302.
- 790 Andres, R. J., Boden, T. A., Bréon, F.-M., Ciais, P., Davis, S., Erickson, D., . . . Miller, J. J. B. (2012). A
791 synthesis of carbon dioxide emissions from fossil-fuel combustion. 9(5), 1845-1871.
- 792 Andres, R. J., Gregg, J. S., Losey, L., Marland, G., Boden, T. A. J. T. B. C., & Meteorology, P. (2011).
793 Monthly, global emissions of carbon dioxide from fossil fuel consumption. 63(3), 309-327.
- 794 Bakwin, P., Davis, K., Yi, C., Wofsy, S., Munger, J., Haszpra, L., & Barcza, Z. (2004). Regional carbon
795 dioxide fluxes from mixing ratio data. *Tellus B*, 56(4), 301-311.
- 796 Ballantyne, A. P., Alden, C. B., Miller, J. B., Tans, P. P., & White, J. W. C. (2012). Increase in observed
797 net carbon dioxide uptake by land and oceans during the past 50 years. *Nature*, 488(7409), 70-
798 +. doi:10.1038/nature11299
- 799 Birol, F. (2010). World energy outlook 2010. *International Energy Agency*.
- 800 Bousquet, P., Ciais, P., Peylin, P., Ramonet, M., & Monfray, P. (1999). Inverse modeling of annual
801 atmospheric CO₂ sources and sinks: 1. Method and control inversion. *Journal of Geophysical*
802 *Research: Atmospheres (1984–2012)*, 104(D21), 26161-26178.
- 803 Breon, F., & Peylin, P. (2003). The potential of spaceborne remote sensing to contribute to the
804 quantification of anthropogenic emissions in the frame of the Kyoto protocol. *ESA Study, Final*
805 *Report*.
- 806 Buchwitz, M., Reuter, M., Schneising, O., Hewson, W., Detmers, R. G., Boesch, H., . . . Wunch, D.
807 (2017). Global satellite observations of column-averaged carbon dioxide and methane: The
808 GHG-CCI XCO₂ and XCH₄ CRDP3 data set. *Remote Sensing of Environment*, 203, 276-295.
809 doi:<https://doi.org/10.1016/j.rse.2016.12.027>
- 810 Connor, B., Bösch, H., McDuffie, J., Taylor, T., Fu, D., Frankenberg, C., . . . Pollock, R. J. A. M. T.
811 (2016). Quantification of uncertainties in OCO-2 measurements of XCO₂: Simulations and
812 linear error analysis. 9(10), 5227-5238.
- 813 Crippa, M., Guizzardi, D., Muntean, M., Schaaf, E., Dentener, F., Van Aardenne, J. A., . . . Pagliari, V. J.
814 E. S. S. D. (2018). Gridded emissions of air pollutants for the period 1970–2012 within EDGAR
815 v4. 3.2. 10(4), 1987-2013.
- 816 Deng, A., Lauvaux, T., Davis, K. J., Gaudet, B. J., Miles, N., Richardson, S. J., . . . Bonin, T. A. J. E. S.
817 A. (2017). Toward reduced transport errors in a high resolution urban CO₂ inversion system. 5,
818 20.
- 819 Ehret, G., Kiemle, C., Wirth, M., Amediek, A., Fix, A., & Houweling, S. (2008). Space-borne remote
820 sensing of CO₂, CH₄, and N₂O by integrated path differential absorption lidar: a sensitivity
821 analysis. *Applied Physics B*, 90(3), 593-608.
- 822 Eldering, A., O'Dell, C. W., Wennberg, P. O., Crisp, D., Gunson, M. R., Viatte, C., . . . Yoshimizu, J.
823 (2017). The Orbiting Carbon Observatory-2: first 18 months of science data products.
824 *Atmospheric Measurement Techniques*, 10(2), 549-563. doi:10.5194/amt-10-549-2017



- 825 Eldering, A., O'Dell, C. W., Wennberg, P. O., Crisp, D., Gunson, M. R., Viatte, C., . . . Chang, A. J. A. M.
826 T. (2017). The Orbiting Carbon Observatory-2: First 18 months of science data products. *10(2)*,
827 549-563.
- 828 Eldering, A., Wennberg, P. O., Crisp, D., Schimel, D. S., Gunson, M. R., Chatterjee, A., . . . Weir, B.
829 (2017). The Orbiting Carbon Observatory-2 early science investigations of regional carbon
830 dioxide fluxes. *Science*, *358*(6360), 188-+. doi:10.1126/science.aam5745
- 831 Fasoli, B., Lin, J. C., Bowling, D. R., Mitchell, L., & Mendoza, D. (2018). Simulating atmospheric tracer
832 concentrations for spatially distributed receptors: updates to the Stochastic Time-Inverted
833 Lagrangian Transport model's R interface (STILT-R version 2). *Geoscientific Model
834 Development*, *11*(7), 2813-2824. doi:10.5194/gmd-11-2813-2018
- 835 Fischer, M. L., Parazoo, N., Brophy, K., Cui, X., Jeong, S., Liu, J., . . . Oda, T. J. J. o. G. R. A. (2017).
836 Simulating estimation of California fossil fuel and biosphere carbon dioxide exchanges
837 combining in situ tower and satellite column observations. *122*(6), 3653-3671.
- 838 Gerbig, C., Lin, J. C., Wofsy, S. C., Daube, B. C., Andrews, A. E., Stephens, B. B., . . . Grainger, C. A.
839 (2003). Toward constraining regional-scale fluxes of CO₂ with atmospheric observations over
840 a continent: 1. Observed spatial variability from airborne platforms. *Journal of Geophysical
841 Research-Atmospheres*, *108*(D24). doi:10.1029/2002jd003018
- 842 Gilfillan, D., & Marland, G. J. E. S. S. D. (2021). CDIAC-FF: global and national CO₂ emissions from
843 fossil fuel combustion and cement manufacture: 1751–2017. *13*(4), 1667-1680.
- 844 Gurney, K. R., Chen, Y. H., Maki, T., Kawa, S. R., Andrews, A., & Zhu, Z. (2005). Sensitivity of
845 atmospheric CO₂ inversions to seasonal and interannual variations in fossil fuel emissions.
846 *Journal of Geophysical Research Atmospheres*, *110*(D10), -.
- 847 Gurney, K. R., Law, R. M., Denning, A. S., Rayner, P. J., Baker, D., Bousquet, P., . . . Yuen, C. W. (2002).
848 Towards robust regional estimates of CO₂ sources and sinks using atmospheric transport models.
849 [提出不同大气传输模式的结果基本一致, 目前的地面通量观测在碳汇的区域分配中存在的
850 的难题]. *Nature*, *415*(6872), 626-630. doi:10.1038/415626a
- 851 Gurney, K. R., Liang, J., O'keeffe, D., Patarasuk, R., Hutchins, M., Huang, J., . . . Song, Y. J. J. o. G. R.
852 A. (2019). Comparison of global downscaled versus bottom - up fossil fuel CO₂ emissions at
853 the urban scale in four US urban areas. *124*(5), 2823-2840.
- 854 Gurney, K. R., Mendoza, D. L., Zhou, Y., Fischer, M. L., Miller, C. C., Geethakumar, S., . . . technology.
855 (2009). High resolution fossil fuel combustion CO₂ emission fluxes for the United States.
856 *43*(14), 5535-5541.
- 857 Gurney, K. R., Razlivanov, I., Song, Y., Zhou, Y., Benes, B., Abdul-Massih, M. J. E. s., & technology.
858 (2012). Quantification of fossil fuel CO₂ emissions on the building/street scale for a large US
859 city. *46*(21), 12194-12202.
- 860 Hakkarainen, J., Ialongo, I., & Tamminen, J. (2016). Direct space - based observations of anthropogenic
861 CO₂ emission areas from OCO - 2. *Geophysical research letters*, *43*(21).
- 862 Han, G., Gong, W., Lin, H., Ma, X., & Xiang, Z. (2015). Study on Influences of Atmospheric Factors on
863 Vertical Profile Retrieving From Ground-Based DIAL at 1.6 μm. *Ieee Transactions on
864 Geoscience and Remote Sensing*, *53*(6), 3221-3234.
- 865 Han, G., Ma, X., Liang, A., Zhang, T., Zhao, Y., Zhang, M., & Gong, W. (2017a). Performance Evaluation
866 for China's Planned CO₂-IPDA. *Remote Sensing*, *9*(8), 768.
- 867 Han, G., Ma, X., Liang, A., Zhang, T., Zhao, Y., Zhang, M., & Gong, W. J. R. S. (2017b). Performance
868 evaluation for China's planned CO₂-IPDA. *9*(8), 768.



- 869 Han, G., Xu, H., Gong, W., Liu, J., Du, J., Ma, X., & Liang, A. (2018). Feasibility Study on Measuring
870 Atmospheric CO₂ in Urban Areas Using Spaceborne CO₂-IPDA LIDAR. *Remote Sensing*,
871 *10*(7), 985.
- 872 Hefner, M., Marland, G., Oda, T. J. M., & Change, A. S. f. G. (2024). The changing mix of fossil fuels
873 used and the related evolution of CO₂ emissions. *29*(6), 1-11.
- 874 Janssens-Maenhout, G., Crippa, M., Guizzardi, D., Muntean, M., Schaaf, E., Dentener, F., . . . Peters, J.
875 A. H. W. (2017). EDGAR v4.3.2 Global Atlas of the three major Greenhouse Gas Emissions for
876 the period 1970–2012. 1-55.
- 877 Jiye, Z. J. (2020). A data-driven upscale product of global gross primary production, net ecosystem
878 exchange and ecosystem respiration.
- 879 Kaminski, T., Scholze, M., Vossbeck, M., Knorr, W., Buchwitz, M., & Reuter, M. (2017). Constraining
880 a terrestrial biosphere model with remotely sensed atmospheric carbon dioxide. *Remote Sensing*
881 *of Environment*, *203*, 109-124. doi:<https://doi.org/10.1016/j.rse.2017.08.017>
- 882 Kawa, S., Mao, J., Abshire, J., Collatz, G., Sun, X., & Weaver, C. (2010). Simulation studies for a space -
883 based CO₂ lidar mission. *Tellus B*, *62*(5), 759-769.
- 884 Kiemle, C., Ehret, G., Amediek, A., Fix, A., Quatrevalet, M., & Wirth, M. (2017). Potential of Spaceborne
885 Lidar Measurements of Carbon Dioxide and Methane Emissions from Strong Point Sources.
886 *Remote Sensing*, *9*(11), 1137.
- 887 Kiemle, C., Kawa, S. R., Quatrevalet, M., & Browell, E. V. (2014). Performance simulations for a
888 spaceborne methane lidar mission. *Journal of Geophysical Research-Atmospheres*, *119*(7),
889 4365-4379. doi:10.1002/2013jd021253
- 890 Kiemle, C., Quatrevalet, M., Ehret, G., Amediek, A., Fix, A., & Wirth, M. (2011). Sensitivity studies for
891 a space-based methane lidar mission. *Atmospheric Measurement Techniques*, *4*(10), 2195-2211.
892 doi:10.5194/amt-4-2195-2011
- 893 Kohler, P., Guanter, L., Kobayashi, H., Walther, S., & Yang, W. (2018). Assessing the potential of sun-
894 induced fluorescence and the canopy scattering coefficient to track large-scale vegetation
895 dynamics in Amazon forests. *Remote Sensing of Environment*, *204*, 769-785.
896 doi:10.1016/j.rse.2017.09.025
- 897 Kort, E. A., Angevine, W. M., Duren, R., & Miller, C. E. (2013). Surface observations for monitoring
898 urban fossil fuel CO₂ emissions: Minimum site location requirements for the Los Angeles
899 megacity. *Journal of Geophysical Research-Atmospheres*, *118*(3), 1-8. doi:10.1002/jgrd.50135
- 900 Lauvaux, T., Miles, N. L., Deng, A., Richardson, S. J., Cambaliza, M. O., Davis, K. J., . . . O'Keefe, D.
901 J. J. o. G. R. A. (2016). High - resolution atmospheric inversion of urban CO₂ emissions during
902 the dormant season of the Indianapolis Flux Experiment (INFLUX). *121*(10), 5213-5236.
- 903 Li, X., Xiao, J. F., & He, B. B. (2018). Chlorophyll fluorescence observed by OCO-2 is strongly related
904 to gross primary productivity estimated from flux towers in temperate forests. *Remote Sensing*
905 *of Environment*, *204*, 659-671. doi:10.1016/j.rse.2017.09.034
- 906 Lin, J., & Gerbig, C. J. G. R. L. (2005). Accounting for the effect of transport errors on tracer inversions.
907 *32*(1).
- 908 Lin, J. C., Gerbig, C., Wofsy, S. C., Andrews, A. E., Daube, B. C., Davis, K. J., & Grainger, C. A. (2003).
909 A near-field tool for simulating the upstream influence of atmospheric observations: The
910 Stochastic Time-Inverted Lagrangian Transport (STILT) model. *Journal of Geophysical*
911 *Research-Atmospheres*, *108*(D16). doi:10.1029/2002jd003161
- 912 Lin, J. C., Gerbig, C., Wofsy, S. C., Andrews, A. E., Daube, B. C., Grainger, C. A., . . . Hollinger, D. Y.



- 913 (2004). Measuring fluxes of trace gases at regional scales by Lagrangian observations:
914 Application to the CO₂ Budget and Rectification Airborne (COBRA) study. *Journal of*
915 *Geophysical Research-Atmospheres*, 109(D15). doi:10.1029/2004jd004754
- 916 Luo, B., Yang, J., Song, S., Shi, S., Gong, W., Wang, A., & Du, L. J. R. S. (2022). Target classification
917 of similar spatial characteristics in complex urban areas by using multispectral LiDAR. *14*(1),
918 238.
- 919 Mahadevan, P., Wofsy, S. C., Matross, D. M., Xiao, X., Dunn, A. L., Lin, J. C., . . . Gottlieb, E. W. J. G.
920 B. C. (2008). A satellite - based biosphere parameterization for net ecosystem CO₂ exchange:
921 Vegetation Photosynthesis and Respiration Model (VPRM). *22*(2).
- 922 Mao, J., Ramanathan, A., Abshire, J. B., Kawa, S. R., Riris, H., Allan, G. R., . . . Numata, K. (2018).
923 Measurement of atmospheric CO₂ column concentrations to cloud tops with a pulsed multi-
924 wavelength airborne lidar. *Atmospheric Measurement Techniques*, 11(1), 1-26.
- 925 Miller, J. B., Tans, P. P., & Gloor, M. (2014). Steps for success of OCO-2. *Nature Geoscience*, 7(10),
926 691-691.
- 927 Miller, J. B., Tans, P. P., & Gloor, M. J. N. G. (2014). Steps for success of OCO-2. 7(10), 691-691.
- 928 Moore III, B., Crowell, S. M., Rayner, P. J., Kumer, J., O'Dell, C. W., O'Brien, D., . . . Lemen, J. J. F. i.
929 E. S. (2018). The potential of the Geostationary Carbon Cycle Observatory (GeoCarb) to
930 provide multi-scale constraints on the carbon cycle in the Americas. *6*, 109.
- 931 Myneni, R. B., Dong, J., Tucker, C. J., Kaufmann, R. K., Kauppi, P. E., Liski, J., . . . Hughes, M. K.
932 (2001). A large carbon sink in the woody biomass of Northern forests. *Proceedings of the*
933 *National Academy of Sciences of the United States of America*, 98(26), 14784-14789.
934 doi:10.1073/pnas.261555198
- 935 Nehr Korn, T., Eluszkiewicz, J., Wofsy, S. C., Lin, J. C., Gerbig, C., Longo, M., & Freitas, S. (2010).
936 Coupled weather research and forecasting-stochastic time-inverted lagrangian transport (WRF-
937 STILT) model. *Meteorology and Atmospheric Physics*, 107(1-2), 51-64. doi:10.1007/s00703-
938 010-0068-x
- 939 Nehr Korn, T., Henderson, J., Leidner, M., Mountain, M., Eluszkiewicz, J., McKain, K., & Wofsy, S.
940 (2013). WRF Simulations of the Urban Circulation in the Salt Lake City Area for CO₂ Modeling.
941 *Journal of Applied Meteorology and Climatology*, 52(2), 323-340. doi:10.1175/jamc-d-12-061.1
- 942 Oda, T., & Maksyutov, S. (2011). A very high-resolution (1 km x 1 km) global fossil fuel CO₂ emission
943 inventory derived using a point source database and satellite observations of nighttime lights.
944 *Atmospheric Chemistry and Physics*, 11(2), 543-556. doi:10.5194/acp-11-543-2011
- 945 Patra, P. K., Hajima, T., Saito, R., Chandra, N., Yoshida, Y., Ichii, K., . . . Science, P. (2021). Evaluation
946 of earth system model and atmospheric inversion using total column CO₂ observations from
947 GOSAT and OCO-2. *8*, 1-18.
- 948 Pei, Z., Han, G., Ma, X., Shi, T., Gong, W. J. I. T. o. G., & Sensing, R. (2022). A method for estimating
949 the background column concentration of CO₂ using the lagrangian approach. *60*, 1-12.
- 950 Pillai, D., Gerbig, C., Kretschmer, R., Beck, V., Karstens, U., Neininger, B., & Heimann, M. (2012).
951 Comparing Lagrangian and Eulerian models for CO₂ transport - a step towards Bayesian inverse
952 modeling using WRF/STILT-VPRM. *Atmospheric Chemistry and Physics*, 12(19), 8979-8991.
953 doi:10.5194/acp-12-8979-2012
- 954 Rayner, P., & O'Brien, D. (2001). The utility of remotely sensed CO₂ concentration data in surface source
955 inversions. *Geophysical research letters*, 28(1), 175-178.
- 956 Refaat, T. F., Singh, U. N., Yu, J., Petros, M., Remus, R., & Ismail, S. J. A. O. (2016). Double-pulse 2-



- 957 um integrated path differential absorption lidar airborne validation for atmospheric carbon
958 dioxide measurement. *55*(15), 4232-4246.
- 959 Reuter, M., Buchwitz, M., Hilker, M., Heymann, J., Schneising, O., Pillai, D., . . . Sawa, Y. (2014).
960 Satellite-inferred European carbon sink larger than expected. *Atmospheric Chemistry and*
961 *Physics*, *14*(24), 13739-13753. doi:10.5194/acp-14-13739-2014
- 962 Roten, D., Lin, J. C., Kunik, L., Mallia, D., Wu, D., Oda, T., . . . Discussions, P. (2022). The information
963 content of dense carbon dioxide measurements from space: a high-resolution inversion approach
964 with synthetic data from the OCO-3 instrument. *2022*, 1-43.
- 965 Schwandner, F. M., Gunson, M. R., Miller, C. E., Carn, S. A., Eldering, A., Krings, T., . . . Podolske, J.
966 R. (2017). Spaceborne detection of localized carbon dioxide sources. *Science*, *358*(6360), 192-
967 +. doi:10.1126/science.aam5782
- 968 Shan, Y., Guan, D., Zheng, H., Ou, J., Li, Y., Meng, J., . . . Zhang, Q. (2018). China CO₂ emission
969 accounts 1997–2015. *Scientific Data*, *5*, 170201. doi:10.1038/sdata.2017.201
970 <https://www.nature.com/articles/sdata2017201#supplementary-information>
- 971 Shan, Y., Liu, J., Liu, Z., Xu, X., Shao, S., Wang, P., & Guan, D. (2016). New provincial CO₂ emission
972 inventories in China based on apparent energy consumption data and updated emission factors.
973 *Applied Energy*, *184*, 742-750. doi:<https://doi.org/10.1016/j.apenergy.2016.03.073>
- 974 Stephens, B. B., Gurney, K. R., Tans, P. P., Sweeney, C., Peters, W., Bruhwiler, L., . . . Nakazawa, T.
975 (2007). Weak northern and strong tropical land carbon uptake from vertical profiles of
976 atmospheric CO₂. *Science*, *316*(5832), 1732-1735.
- 977 Sun, Y., Frankenberg, C., Jung, M., Joiner, J., Guanter, L., Kohler, P., & Magney, T. (2018). Overview of
978 Solar-Induced chlorophyll Fluorescence (SIF) from the Orbiting Carbon Observatory-2:
979 Retrieval, cross-mission comparison, and global monitoring for GPP. *Remote Sensing of*
980 *Environment*, *209*, 808-823. doi:10.1016/j.rse.2018.02.016
- 981 Tomohiro Oda, S. M. (2015). ODIAC Fossil Fuel CO₂ Emissions Dataset(ODIAC2023).
982 doi:10.17595/20170411.001.
- 983 Toon, G., Blavier, J.-F., Washenfelder, R., Wunch, D., Keppel-Aleks, G., Wennberg, P., . . . Deutscher, N.
984 (2009). *Total column carbon observing network (TCCON)*. Paper presented at the Hyperspectral
985 Imaging and Sensing of the Environment.
- 986 Turner, A. J., Jacob, D. J., Benmergui, J., Brandman, J., White, L., & Randles, C. A. (2018). Assessing
987 the capability of different satellite observing configurations to resolve the distribution of
988 methane emissions at kilometer scales. *Atmospheric Chemistry and Physics*, *18*(11), 8265-8278.
989 doi:10.5194/acp-18-8265-2018
- 990 Van der Werf, G. R., Randerson, J. T., Giglio, L., Collatz, G., Mu, M., Kasibhatla, P. S., . . . physics.
991 (2010). Global fire emissions and the contribution of deforestation, savanna, forest, agricultural,
992 and peat fires (1997–2009). *10*(23), 11707-11735.
- 993 Vogel, F. R., Thiruchittampalam, B., Theloke, J., Kretschmer, R., Gerbig, C., Hammer, S., & Levin, I.
994 (2013). Can we evaluate a fine-grained emission model using high-resolution atmospheric
995 transport modelling and regional fossil fuel CO₂ observations? *Tellus Series B-Chemical and*
996 *Physical Meteorology*, *65*. doi:10.3402/tellusb.v65i0.18681
- 997 Wang, H., Jiang, F., Wang, J., Ju, W., Chen, J. M. J. A. C., & Physics. (2019). Terrestrial ecosystem
998 carbon flux estimated using GOSAT and OCO-2 XCO₂ retrievals. *19*(18), 12067-12082.
- 999 Wang, J., Kawa, S., Eluszkiewicz, J., Baker, D., Mountain, M., Henderson, J., . . . Physics. (2014). A
1000 regional CO₂ observing system simulation experiment for the ASCENDS satellite mission.



- 1001 *14*(23), 12897-12914.
- 1002 Wang, J. S., Kawa, S. R., Eluszkiewicz, J., Baker, D. F., Mountain, M., Henderson, J., . . . Zaccheo, T. S.
- 1003 (2014). A regional CO₂ observing system simulation experiment for the ASCENDS satellite
- 1004 mission. *Atmospheric Chemistry and Physics*, *14*(23), 12897-12914. doi:10.5194/acp-14-
- 1005 12897-2014
- 1006 Wang, Q., Mustafa, F., Bu, L., Zhu, S., Liu, J., & Chen, W. J. A. M. T. (2021). Atmospheric carbon
- 1007 dioxide measurement from aircraft and comparison with OCO-2 and CarbonTracker model data.
- 1008 *14*(10), 6601-6617.
- 1009 Watson, A. J., Schuster, U., Bakker, D. C. E., Bates, N. R., Corbiere, A., Gonzalez-Davila, M., . . .
- 1010 Wanninkhof, R. (2009). Tracking the Variable North Atlantic Sink for Atmospheric CO₂.
- 1011 *Science*, *326*(5958), 1391-1393. doi:10.1126/science.1177394
- 1012 Wu, D., Lin, J. C., Duarte, H. F., Yadav, V., Parazoo, N. C., Oda, T., & Kort, E. A. (2021). A model for
- 1013 urban biogenic CO₂ fluxes: Solar-Induced Fluorescence for Modeling Urban biogenic Fluxes
- 1014 (SMUrF v1). *Geosci. Model Dev.*, *14*(6), 3633-3661. doi:10.5194/gmd-14-3633-2021
- 1015 Xiang, C., Ma, X., Zhang, X., Han, G., Zhang, W., Chen, B., . . . Sensing, R. (2021). Design of inversion
- 1016 procedure for the airborne CO₂-IPDA LIDAR: A preliminary study. *14*, 11840-11852.
- 1017 Ye, X., Lauvaux, T., Kort, E. A., Oda, T., Feng, S., Lin, J. C., . . . Wu, D. J. J. o. G. R. A. (2020).
- 1018 Constraining fossil fuel CO₂ emissions from urban area using OCO - 2 observations of total
- 1019 column CO₂. *125*(8), e2019JD030528.
- 1020 Zhang, H., Han, G., Chen, W., Pei, Z., Liu, B., Liu, J., . . . Sensing, R. (2024). Validation Method for
- 1021 Spaceborne IPDA LIDAR X co 2 Products via TCCON.
- 1022 Zhu, Y., Liu, J., Chen, X., Zhu, X., Bi, D., & Chen, W. J. O. E. (2019). Sensitivity analysis and correction
- 1023 algorithms for atmospheric CO₂ measurements with 1.57- μ m airborne double-pulse IPDA
- 1024 LIDAR. *27*(22), 32679-32699.
- 1025 Zhu, Y., Yang, J., Chen, X., Zhu, X., Zhang, J., Li, S., . . . Bu, L. J. R. S. (2020). Airborne validation
- 1026 experiment of 1.57- μ m double-pulse IPDA LIDAR for atmospheric carbon dioxide
- 1027 measurement. *12*(12), 1999.
- 1028